ACCSCIENCE PUBLISHING
An International Journal of Optimization and Control: Theories & Applications
ISSN: 2146-0957 eISSN: 2146-5703
Vol.16, No.1, pp.91-110 (2026)
https://doi.org/10.36922/IJOCTA025320140
IJOCTA

RESEARCH ARTICLE

Existence and uniqueness analysis of a fractional atmospheric system using Haar-based operational matrices

Mumtaz Ali[1,2], Najeeb Alam Khan[1*], Muhammad Ayaz[1], and Nadeem Alam Khan[3]

[1]Department of Mathematics, University of Karachi, Karachi, Sindh, Pakistan
[2]Basic Sciences Department, Balochistan University of Engineering Technology, Khuzdar, Balochistan, Pakistan
[3]Department of Computer Sciences, Iqra University, Karachi, Sindh, Pakistan
mumtaz.ali@buetk.edu.pk, njbalam@yahoo.com, ayaz_maths@hotmail.com, nadeemalamkhan.pk@gmail.com

ARTICLE INFO

Article History:
Received: August 4, 2025
Revised: September 22, 2025
Accepted: September 26, 2025
Published Online: November 6, 2025

Keywords:
Atmospheric model
Atangana-Baleanu-Caputo derivative
Haar wavelet
Operational matrix
Existence and uniqueness

ABSTRACT

Understanding and accurately modeling the dynamics of climate-related processes is essential for predicting and mitigating the effects of global warming. This study introduces a fractional order atmospheric model that simultaneously captures the interactions among three key variables: permafrost thaw, atmospheric temperature, and greenhouse gas concentration. The model was formulated using the Atangana–Baleanu–Caputo fractional derivative, allowing for the inclusion of memory effects that are critical in climate dynamics. To solve the resulting nonlinear fractional differential equations, we constructed an operational matrix of the Atangana–Baleanu fractional integral operator based on Haar wavelets. Using Haar series expansions and operational matrices, the system was transformed into an objective function. This objective function was then minimized using differential evolution optimization to determine unknown Haar coefficients. The proposed method was validated against traditional numerical and predictor–corrector methods, with theoretical analysis confirming existence, uniqueness, and a provable upper bound for the approximation error. Numerical experiments under various parameter settings demonstrated the high accuracy, efficiency, and flexibility of the method. These results highlight the potential of fractional order modeling as a powerful framework for analyzing complex environmental systems and improving climate prediction models.

1. Introduction

The origins of fractional calculus (FC) can be traced back to the 17th century when Newton and Leibniz laid its foundational concepts. The concept of derivatives of arbitrary order was formally considered by Lacroix in 1819. Fractional models are based on fractional differential equations (FDEs) that involve derivatives of non-integer order.[1] These models are widely recognized for their effectiveness in capturing complex system behaviors more accurately than the classical integer-order approaches. The importance of FC lies in its ability to describe memory and hereditary properties of various materials and processes, which are often neglected by classical models. Moreover, FDE-based models offer better flexibility and precision in fitting experimental data, leading to improved predictions and deeper physical insights.[2,3]

Various definitions of fractional derivatives have been developed over the years. Notably, in 1967, Caputo introduced a derivative definition whose structure closely resembled that of the classical integer-order derivative, making it more suitable for initial value problems and real-world applications. Since the early 2000s, there has been growing interest in mathematical analysis,

*Corresponding Author

numerical methods, and optimization techniques for FDEs.[4] FC has proven to be especially effective in modeling phenomena across diverse domains such as biology,[5,6] environmental science,[7] economics,

In recent years, attention has shifted to non-singular and non-local definitions of fractional derivatives, such as the Atangana–Baleanu–Caputo (ABC) derivative.[11] This operator addresses some of the limitations of classical definitions (e.g., Riemann Liouville (RL) and Caputo), which often involve singular (free from singularities at the origin) and non-local (accounting for the entire history of the function). For instance, in the Rabinovich system, the ABC fractional model delays the onset of chaos relative to the Caputo model, reflecting different memory accumulation and loss in the two formulations.[12] Further, comparative analysis of integral operator RL vs. Caputo Fabrizio vs. ABC shows that Atangana–Baleanu integrals, with their non-singular Mittag–Leffler kernel, assign smoother decays to historical contributions, offering more flexible control over memory effects and avoiding some of the singularities that arise in power law kernel operators.[13] Global warming poses a significant threat to ecosystems worldwide, with one of its most direct consequences being permafrost thawing.[14] Permafrost, which covers nearly one fourth of Earth's land area and is concentrated in the northern hemisphere, including the regions of Alaska, Russia, and Canada, consists of soil, rock, and ice that remain frozen for at least 2 years.[15] This frozen ground stores immense quantities of undecomposed organic matter and even ancient microorganisms 400,000 years. Above it lies a seasonal active layer that regulates ecological balance and supports infrastructure.[16] Rising Arctic temperatures, nearly twice the global average, are accelerating permafrost degradation, releasing greenhouse gases such as methane and carbon dioxide that amplify global warming through positive feedback.[17] Furthermore, as permafrost thaws, dormant pathogens and ancient microbes preserved in the ice may become active. Some of these biological agents have been implicated in the death of wildlife, including muskoxen, reindeer, caribou, and bird population in Siberia.

Permafrost, a critical component of the cryosphere, is increasingly vulnerable to global climate change. Pan et al.[18] demonstrated the intricate dynamics of Lorenz energy cycling in the global atmosphere, providing a framework for understanding climate-related processes that influence permafrost regions. Increasing soil temperatures and thaw depths significantly impact the biodegradability of organic carbon stored within permafrost, a phenomenon corroborated by studies such as Mu et al.[19] In the Northern Hemisphere, numerous human settlements built on permafrost face substantial risks because thawing undermines critical infrastructure. Projections indicate that 20–70% of permafrost could melt by 2100, potentially releasing an estimated 10–100 Gt of carbon into the atmosphere, thereby exacerbating climate change. Wang et al.[20] highlighted the significant role of elevation in influencing thaw depth and nutrient runoff, while Cui et al.[21] documented infrastructure-related permafrost degradation in the ecologically sensitive Qinghai Tibet corridor. Recognizing these profound environmental shifts, growing public awareness is fostering increased adoption of environmentally sustainable practices, although the scale of the permafrost challenge requires more comprehensive interventions.

In this study, we investigate a nonlinear atmospheric model22 within the ABC framework.

$$\begin{aligned} {}_0^{ABC}D_\varsigma^\varphi f(\varsigma) &= -af(\varsigma) + bg(\varsigma) + \alpha_1 E(\varsigma), \\ {}_0^{ABC}D_\varsigma^\varphi g(\varsigma) &= -\eta g(\varsigma) + \xi f(\varsigma) h(\varsigma) + \mu f^3(\varsigma) \\ &\quad + \alpha_2 E(\varsigma), \\ {}_0^{ABC}D_\varsigma^\varphi h(\varsigma) &= -\sigma h(\varsigma) + \lambda f(\varsigma) g(\varsigma) - \beta h^2(\varsigma) \\ &\quad + \alpha_3 E(\varsigma). \end{aligned} \tag{1}$$

with initial conditions

$$f(0) = w_1,\ g(0) = w_2,\ h(0) = w_3. \tag{2}$$

.

In this model, the ABC fractional derivative of order φ, where $0 < \varphi \leq 1$, is employed and denoted ${}_0^{ABC}D_\varsigma^\varphi$. The function $f(\varsigma)$describes the permafrost thaw dynamics, which can be related to measurable variables such as thaw depth m, soil temperature profiles, or active layer thickness obtained from field data and remote sensing observations. The function $g(\varsigma)$represents atmospheric temperature, expressed in degrees Celsius ($^\circ C$), which is a directly measurable climate variable through meteorological stations or reanalysis. The function $h(\varsigma)$ denotes greenhouse gas emissions, which can be quantified in parts per million for CO_2 using atmospheric monitoring records. A sinusoidal external forcing term $E(\varsigma)$ has been introduced in all three components of the model to present periodic seasonal variations, such as annual cycles of solar radiation or temperature fluctuations. The model incorporates several parameters, namely, $a, b, \eta, \xi, \mu, \sigma, \lambda, \beta, \alpha_1, \alpha_2, \alpha_3$ which are treated as constants. Specifically, parameter corresponds

to the subsurface temperature at which water freezes and forms permafrost, whereas indicates the depth at which permafrost begins to thaw due to increasing temperature. Coefficient ξ characterizes the growth rate of the temperature, whereas η signifies its depletion rate. The variable μ accounts for the temperature increase attributed to the elevated greenhouse gas concentrations. Additionally, σ and λ represent the natural rates of greenhouse gas reduction and emission, β indicates the effectiveness of implemented measures aimed at controlling greenhouse gas emissions and $\alpha_1, \alpha_2, \alpha_3$ are scaling coefficients representing the sensitivity of each variable to external forcing terms.

Researchers have proposed several methods to model nonlinear atmospheric systems. Agrawal et al.[22] employed Bernoulli polynomials to obtain solutions for a fractional atmospheric model formulated in Caputo sense, while Yeshwanth et al.[23] employed a modified Hermit wavelet collocation approach for similar problems. Naik et al.[24] designed a fractional order atmospheric model using a class of ACT-like chaotic system and developed its sliding mode chaos control. More recently, wavelet based approaches have gained popularity for solving nonlinear differential equations due to their ability to provide sparse and efficient representations. For instance, Ahmed et al.[25] developed a Fibonacci wavelet method to investigate physical problems, demonstrating its computational efficiency. Similarly, Khan et al.[26] solved scalar reaction diffusion equations with cubic nonlinearity and time dependent coefficients using the wavelet method of lines. These contributions highlight the versatility and growing interest in wavelet methods for solving complex nonlinear systems.

Building on this progress, our study focuses on the flexibility of wavelet theory, a powerful mathematical tool well known for its ability to represent continuous functions in multiple resolutions. Beyond its applications in signal decomposition and image processing, wavelet theory has been successfully employed for solving differential and fraction differential equations.[27] Multi-resolution wavelets employ a hierarchical design to build successive levels of resolution. The fundamental elements of this vector space are called wavelet scaling functions, which are characterized by their integral basis and orthogonal properties.[28] Among the many wavelet families introduced over time, the Haar wavelets (HWs) are considered the simplest. First introduced by Alfred Haar in 1910, HWs are a special case of Daubechies wavelets of order 1 characterized by their constant values of 1, 1, and 0. Owing to their simplicity, HWs are widely used in various applications and offer fast, efficient, and computationally attractive solutions. A major advantage of HWs is their ability to transform differential equations into systems of algebraic equations without the need for residual or product operational matrices, thereby reducing computational complexity. Kumar et al.[29] used the HW method to study the fractional Lotka–Volterra model in Caputo sense. Khan et al.[30] developed an HW operational matrix method to solve pantograph FDEs in Atangana's beta derivative sense. Saeed[31] applied a modified HW approach to solve linear and nonlinear variable order fractional diffusion type equations in Caputo sense. Additional studies on similar approaches can be found in Refs.[31,32] Building on the efficiency and simplicity of HWs, we extend their application to fractional order modeling within the ABC framework, aiming to address the lack of an operational matrix method for nonlinear atmospheric systems.

Despite significant progress, most existing fractional atmospheric models rely on integer order or Caputo derivatives, which do not fully capture long-term memory effects. Furthermore, many available numerical methods, such as predictor–corrector method (PCM) and the spectral collocation method, suffer from high computational cost and are not easily adaptable to parallel computing environments. To bridge this gap, we develop a Haar wavelet operational matrix method (HWOMM) tailored for the ABC derivative. This framework reduces computational complexity and enhances the potential for parallelization, making it well-suited for large-scale nonlinear systems. The proposed method transforms the governing equations into an objective function using Haar series expansions and a derived operational matrix. The objective function is then minimized using differential evolution optimization to recover the unknown Haar coefficients and reconstruct the solution. The numerical outcomes of HWOMM are compared with those of PCM[33] and NDSolve. We also investigated theoretical properties, such as the existence and uniqueness of the solution. Additionally, the performance measures of the approach are evaluated using statistical indicators such as the root mean square error (RMSE), and error in Nash Sutcliffe efficiency (ENSE).

2. Preliminaries

Definition 1 Let $f \in H^n(a,b)$, $b < a$ and $\varphi \in (n-1, n]$ where a is not necessarily differentiable.

Then, the Atangana–Baleanu fractional derivative in the RL sense, with initial point is defined at any point as follows[11]:

$$\begin{aligned} {}_0^{ABR}D_\varsigma^\varphi f(\varsigma) =& \frac{Q(\varphi)}{1-\varphi}\frac{d^n}{d\varsigma^n}\int_a^\varsigma f(\tau) \\ & E_\varphi\left(-\frac{\varphi}{1-\varphi}(\varsigma-\tau)^\varphi\right)d\tau, \end{aligned} \tag{3}$$

where is the normalization function given by $Q(\varphi) = 1-\varphi+\frac{\varphi}{\Gamma(\varphi)}$.

Definition 2 If $f \in H^n(a,b)$, $b < a$ and $\varphi \in (n-1,n]$, while is not necessarily differentiable, then the Atangana–Baleanu fractional derivative in Caputo sense, with initial point is defined at any point as follows11:

$$\begin{aligned} {}_0^{ABC}D_\varsigma^\varphi f(\varsigma) =& \frac{Q(\varphi)}{1-\varphi}\int_a^\varsigma \frac{d^n f(\tau)}{d\tau^n} \\ & E_\varphi\left(-\frac{\varphi}{1-\varphi}(\varsigma-\tau)^\varphi\right)d\tau, \end{aligned} \tag{4}$$

where $E_\varphi(\varsigma) = \sum_{n=0}^{\infty}\frac{\varsigma^n}{\Gamma(n\varphi+1)}$ is the Mittag–Leffler function.

Definition 3 The Atangana–Baleanu fractional integral of order is given by Ref.[11]:

$$\begin{aligned} {}_a^{AB}I_\varsigma^\varphi f(\varsigma) =& \frac{1-\varphi}{Q(\varphi)}f(\varsigma) + \frac{\varphi}{Q(\varphi)\Gamma(\varphi)} \\ & \int_a^\varsigma (\varsigma-\tau)^{\varphi-1} f(\tau)\,d\tau. \end{aligned} \tag{5}$$

Lemma 1[34] For $0 < \varphi \le 1$, we have

$$\left({}_a^{AB}I_\varsigma^\varphi\, {}_0^{ABC}D_\varsigma^\varphi f\right)(\varsigma) = f(\varsigma) - f(a).$$

3. Existence and uniqueness of the solution

In this section, we establish the existence and uniqueness of the solution to Equation (1) within the ABC framework. We considered the atmospheric model as follows:

$$\begin{aligned} {}_0^{ABC}D_\varsigma^\varphi f(\varsigma) =& -af(\varsigma) + bg(\varsigma) + \alpha_1 E(\varsigma), \\ {}_0^{ABC}D_\varsigma^\varphi g(\varsigma) =& -\eta g(\varsigma) + \xi f(\varsigma)h(\varsigma) + \mu f^3(\varsigma) \\ & + \alpha_2 E(\varsigma), \\ {}_0^{ABC}D_\varsigma^\varphi h(\varsigma) =& -\sigma h(\varsigma) + \lambda f(\varsigma)g(\varsigma) - \beta h^2(\varsigma) \\ & + \alpha_3 E(\varsigma). \end{aligned} \tag{6}$$

We can formulate the proposed system as follows:

$$\begin{aligned} {}_0^{ABC}D_\varsigma^\varphi f(\varsigma) &= L(\varsigma,f,g,h), \\ {}_0^{ABC}D_\varsigma^\varphi g(\varsigma) &= W(\varsigma,f,g,h), \\ {}_0^{ABC}D_\varsigma^\varphi h(\varsigma) &= E(\varsigma,f,g,h), \end{aligned} \tag{7}$$

where

$$\begin{aligned} L(\varsigma,f,g,h) =& -af(\varsigma) + bg(\varsigma) + \alpha_1 E(\varsigma) \\ W(\varsigma,f,g,h) =& -\eta g(\varsigma) + \xi f(\varsigma)h(\varsigma) + \mu f^3(\varsigma) \\ & + \alpha_2 E(\varsigma), \\ E(\varsigma,f,g,h) =& -\sigma h(\varsigma) + \lambda f(\varsigma)g(\varsigma) - \beta h^2(\varsigma) \\ & + \alpha_3 E(\varsigma). \end{aligned} \tag{8}$$

Lemma 2 System of FDES in Equation (7) can be transformed into an equivalent system of integral equations by integrating both sides as follows:

$$\begin{aligned} f(\varsigma) =& f(0) + \frac{1-\varphi}{Q(\varphi)}L(\varsigma,f,g,h) + \frac{\varphi}{Q(\varphi)\Gamma(\varphi)} \\ & \int_0^\varsigma (\varsigma-\tau)^{\varphi-1}L(\tau,f,g,h)\,d\tau, \\ g(\varsigma) =& g(0) + \frac{1-\varphi}{Q(\varphi)}W(\varsigma,f,g,h) + \frac{\varphi}{Q(\varphi)\Gamma(\varphi)} \\ & \int_0^\varsigma (\varsigma-\tau)^{\varphi-1}W(\tau,f,g,h)\,d\tau, \\ h(\varsigma) =& h(0) + \frac{1-\varphi}{Q(\varphi)}E(\varsigma,f,g,h) + \frac{\varphi}{Q(\varphi)\Gamma(\varphi)} \\ & \int_0^\varsigma (\varsigma-\tau)^{\varphi-1}E(\tau,f,g,h)\,d\tau, \end{aligned} \tag{9}$$

For convenience, we can write Equation (9) as:

$$\begin{aligned} \Im(\varsigma) =& \rho_\sigma + \frac{1-\varphi}{Q(\varphi)}\Upsilon(\varsigma,\Im(\varsigma)) + \frac{\varphi}{Q(\varphi)\Gamma(\varphi)} \\ & \int_0^\varsigma (\varsigma-\upsilon)^{\varphi-1}\Upsilon(\upsilon,\Im(\upsilon))\,d\upsilon, \end{aligned}$$

where

$$\Im(\varsigma) = \begin{cases} f(\varsigma) \\ g(\varsigma) \\ h(\varsigma) \end{cases}, \Im(0) = \rho_\sigma = \begin{cases} f(0) = \rho_1 \\ g(0) = \rho_2 \\ h(0) = \rho_3 \end{cases},$$

$$\Upsilon(\varsigma,\Im(\varsigma)) = \begin{cases} L(\varsigma,f,g,h) \\ W(\varsigma,f,g,h) \\ E(\varsigma,f,g,h) \end{cases}.$$

For $\varsigma \in [0,T] \subset R$, if $\Im(\varsigma)$ is a solution to Equation (9), it satisfies Equation (1).

Remark 1 Let $M = C([0,T],\|.\|)$ be the space of all continuous functions defined on the interval$[0,T]$, equipped with the norm $\|.\|$. This forms a normed vector space under the given norm: $\|\Im(\varsigma)\| = \max_{\varsigma\in[0,T]}|\Im(\varsigma)|$.

Lemma 3 Assume that $\Im : [0,T]\times R^N \to R$ is a sequence of continuous functions, and there exists a constant $K > 0$such that $\Im$ satisfies the Lipschitz condition:

$$\left\|\Upsilon\left(\varsigma,\Im\left(\varsigma\right)\right)-\Upsilon\left(\varsigma,\bar{\Im}\left(\varsigma\right)\right)\right\|\leq K\left\|\Im\left(\varsigma\right)-\bar{\Im}\left(\varsigma\right)\right\|, \tag{10}$$

where $\Im\left(\varsigma\right),\bar{\Im}\left(\varsigma\right)\in R$.

Theorem 1 If the specified conditions are met:
(i) Let:

$$\varpi=\left\|\rho_{\sigma}\right\|, U=\sup_{\varsigma\in[0,T]}\left\|\Upsilon\left(\varsigma,0\right)\right\|, \text{and}$$

$$\phi=\frac{1-\varphi}{Q\left(\varphi\right)}+\frac{T^{\varphi}}{Q\left(\varphi\right)\Gamma\left(\varphi\right)}.$$

(ii) The function $\Omega\left(\varsigma,\Im\left(\varsigma\right)\right)$ satisfies a Lipschitz condition in$\Im$:

$$\left\|\Upsilon\left(\varsigma,\Im\left(\varsigma\right)\right)-\Upsilon\left(\varsigma,\bar{\Im}\left(\varsigma\right)\right)\right\|\leq K\left\|\Im\left(\varsigma\right)-\bar{\Im}\left(\varsigma\right)\right\|,$$

(iii) There exist $0<\delta<1$, such that $K\phi\leq\delta<1$. Then, Equation (1) has a unique solution$\Im\left(\varsigma\right)\in M$.

Proof Let us define mapping $\chi:M\rightarrow M$by

$$\chi\Im\left(\varsigma\right)=\rho_{\sigma}+\frac{1-\varphi}{Q\left(\varphi\right)}\Upsilon\left(\varsigma,\Im\left(\varsigma\right)\right)+\frac{\varphi}{Q\left(\varphi\right)\Gamma\left(\varphi\right)}\int_{0}^{\varsigma}\left(\varsigma-\upsilon\right)^{\varphi-1}\Upsilon\left(\upsilon,\Im\left(\upsilon\right)\right)d\upsilon. \tag{11}$$

Let $B_{\mu}:=\left\{\Im\in M:\left\|\Im\right\|\leq\mu\right\}$be a closed ball in , and choose $\mu\geq\frac{\varpi+U\phi}{1-K\phi}$ such that we can show$\chi B_{\mu}\subset B_{\mu}$. Then we have

$$\left\|\chi\Im\left(\varsigma\right)\right\|=\left\|\rho_{\sigma}+\frac{1-\varphi}{Q\left(\varphi\right)}\Upsilon\left(\varsigma,\Im\left(\varsigma\right)\right)+\frac{\varphi}{Q\left(\varphi\right)\Gamma\left(\varphi\right)}\int_{0}^{\varsigma}\left(\varsigma-\upsilon\right)^{\varphi-1}\Upsilon\left(\upsilon,\Im\left(\upsilon\right)\right)d\upsilon,\right.$$

$$\leq\left\|\rho_{\sigma}\right\|+\frac{1-\varphi}{Q\left(\varphi\right)}\left\|\Upsilon\left(\varsigma,\Im\left(\varsigma\right)\right)\right\|+\frac{\varphi}{Q\left(\varphi\right)\Gamma\left(\varphi\right)}\int_{0}^{\varsigma}\left(\varsigma-\upsilon\right)^{\varsigma-1}\left\|\Upsilon\left(\varsigma,\Im\left(\varsigma\right)\right)\right\|d\upsilon,$$

$$=\varpi+\frac{1-\varphi}{Q\left(\varphi\right)}\left\|\Upsilon\left(\varsigma,\Im\left(\varsigma\right)\right)-\Upsilon\left(\varsigma,0\right)+\Upsilon\left(\varsigma,0\right)\right\|$$

$$+\frac{\varphi}{Q\left(\varphi\right)\Gamma\left(\varphi\right)}\int_{0}^{\varsigma}\left(\varsigma-\upsilon\right)^{\varphi-1}\left(\left\|\Upsilon\left(\varsigma,\Im\left(\varsigma\right)\right)-\right.\right.$$

$$\left.\left.\Upsilon\left(\varsigma,0\right)+\Upsilon\left(\varsigma,0\right)\right\|d\upsilon,\right.$$

$$\leq\varpi+\frac{1-\varphi}{Q\left(\varphi\right)}\left\|\Upsilon\left(\varsigma,\Im\left(\varsigma\right)\right)-\Upsilon\left(\varsigma,0\right)\right\|+\left\|\Upsilon\left(\varsigma,0\right)\right\|$$

$$+\frac{\varphi}{Q\left(\varphi\right)\Gamma\left(\varphi\right)}\int_{0}^{\varsigma}\left(\varsigma-\upsilon\right)^{\varphi-1}\left(\left\|\Upsilon\left(\varsigma,\Im\left(\varsigma\right)\right)-\Upsilon\left(\varsigma,0\right)\right\|\right.$$

$$\left.+\left\|\Upsilon\left(\varsigma,0\right)\right\|d\upsilon,\right.$$

$$\leq\varpi+\frac{1-\varphi}{Q\left(\varphi\right)}\left(K\mu+U\right)+\frac{\varphi}{Q\left(\varphi\right)\Gamma\left(\varphi\right)}\int_{0}^{\varsigma}\left(\varsigma-\upsilon\right)^{\varphi-1}\left(K\mu+U\right)d\upsilon,$$

$$\leq\varpi+\frac{1-\varphi}{Q\left(\varphi\right)}\left(K\mu+U\right)+\frac{T^{\varphi}}{Q\left(\varphi\right)\Gamma\left(\varphi\right)}\left(K\mu+U\right),$$

$$\leq\varpi+\left(\frac{1-\varphi}{Q\left(\varphi\right)}+\frac{T^{\varphi}}{Q\left(\varphi\right)\Gamma\left(\varphi\right)}\right)\left(K\mu+U\right),$$

$$\leq\varpi+\phi K\mu+\phi U,$$

$$\leq\mu. \tag{12}$$

This implies that χ maps the set B_{μ} into itself. Consequently, B_{μ} is a complete metric space.

Moreover, for any two functions $\Im\left(\varsigma\right)$ and $\bar{\Im}\left(\varsigma\right)$belonging to B_{μ}, the following holds.

$$\left\|\chi\Im\left(\varsigma\right)-\chi\bar{\Im}\left(\varsigma\right)\right\|=\max_{\varsigma\in[0,T]}\left|\chi\Im\left(\varsigma\right)-\chi\bar{\Im}\left(\varsigma\right)\right|$$

$$=\max_{\varsigma\in[0,T]}\left|\left(\rho_{\sigma}+\frac{1-\varphi}{Q\left(\varphi\right)}\Upsilon\left(\varsigma,\Im\left(\varsigma\right)\right)+\frac{\varphi}{Q\left(\varphi\right)\Gamma\left(\varphi\right)}\right.\right.$$

$$\int_{0}^{\varsigma}\left(\varsigma-\upsilon\right)^{\varphi-1}\Upsilon\left(\upsilon,\Im\left(\upsilon\right)\right)d\upsilon$$

$$\left.-\left(\rho_{\sigma}+\frac{1-\varphi}{Q\left(\varphi\right)}\Upsilon\left(\varsigma,\bar{\Im}\left(\varsigma\right)\right)+\frac{\varphi}{Q\left(\varphi\right)\Gamma\left(\varphi\right)}\right.\right.$$

$$\left.\int_{0}^{\varsigma}\left(\varsigma-\upsilon\right)^{\varphi-1}\Upsilon\left(\upsilon,\bar{\Im}\left(\upsilon\right)\right)d\upsilon,\right.$$

$$=\max_{\varsigma\in[0,T]}\left|\frac{1-\varphi}{Q\left(\varphi\right)}\left(\Upsilon\left(\varsigma,\Im\left(\varsigma\right)\right)-\Upsilon\left(\varsigma,\bar{\Im}\left(\varsigma\right)\right)\right)\right.$$

$$+\frac{\varphi}{Q\left(\varphi\right)\Gamma\left(\varphi\right)}\int_{0}^{\varsigma}\left(\varsigma-\upsilon\right)^{\varphi-1}\left(\Upsilon\left(\upsilon,\Im\left(\upsilon\right)\right)\right.$$

$$\left.-\Upsilon\left(\upsilon,\bar{\Im}\left(\upsilon\right)\right)d\upsilon\right.$$

$$\leq\max_{\varsigma\in[0,T]}\left|\frac{1-\varphi}{Q\left(\varphi\right)}\max_{\varsigma\in[0,T]}\left|\left(\Upsilon\left(\varsigma,\Im\left(\varsigma\right)\right)-\Upsilon\left(\varsigma,\bar{\Im}\left(\varsigma\right)\right)\right)\right|\right.$$

$$+\frac{\varphi}{Q\left(\varphi\right)\Gamma\left(\varphi\right)}\int_{0}^{\varsigma}\left(\varsigma-\upsilon\right)^{\varphi-1}\max_{\upsilon\in[0,\varsigma]}\left|\left(\Upsilon\left(\upsilon,\Im\left(\upsilon\right)\right)\right.\right.$$

$$\left.\left.-\Upsilon\left(\upsilon,\bar{\Im}\left(\upsilon\right)\right)d\upsilon,\right.\right.$$

$$\leq\max_{\varsigma\in[0,T]}\left|\frac{1-\varphi}{Q\left(\varphi\right)}K\left\|\left(\Im\left(\varsigma\right)-\bar{\Im}\left(\varsigma\right)\right)\right\|+\frac{\varphi}{Q\left(\varphi\right)\Gamma\left(\varphi\right)}\right.$$

$$\int_{0}^{\varsigma}\left(\varsigma-\upsilon\right)^{\varphi-1}K\left\|\left(\Im\left(\varsigma\right)-\bar{\Im}\left(\varsigma\right)\right)\right\|d\upsilon,$$

$$=K\left\|\left(\Im\left(\varsigma\right)-\bar{\Im}\left(\varsigma\right)\right)\right\|\left(\frac{1-\varphi}{Q\left(\varphi\right)}+\frac{\varphi}{Q\left(\varphi\right)\Gamma\left(\varphi\right)}\max_{\varsigma\in[0,T]}\right.$$

$$\left.\int_{0}^{\varsigma}\left(\varsigma-\upsilon\right)^{\varphi-1}d\upsilon,\right.$$

$$\leq K\left\|\left(\Im\left(\varsigma\right)-\bar{\Im}\left(\varsigma\right)\right)\right\|\left(\frac{1-\varphi}{Q\left(\varphi\right)}+\frac{T^{\varphi}}{Q\left(\varphi\right)\Gamma\left(\varphi\right)}\right),$$

$$=K\phi\left\|\left(\Im\left(\varsigma\right)-\bar{\Im}\left(\varsigma\right)\right)\right\|,$$

$$\leq\delta\left\|\left(\Im\left(\varsigma\right)-\bar{\Im}\left(\varsigma\right)\right)\right\|. \tag{13}$$

Given that $0<\delta<1$, mapping χ is a contraction. According to Banach's fixed-point

theorem,[35] χ admits a unique fixed-point. Consequently, Equation (6) has a unique solution$\Im(\varsigma) \in M$. This concludes the proof.

4. Haar wavelets and operational matrix

4.1. Haar wavelets

The HW system over the interval $[0,T]$ consists of two foundational components: father and mother wavelets. These basis functions are formally defined as follows[36]:

$$\psi_0(\varsigma) = \begin{cases} 1, & 0 \le \varsigma < T, \\ 0, & \text{otherwise}, \end{cases} \quad \text{and}$$

$$\psi_1(\varsigma) = \begin{cases} 1, & 0 \le \varsigma < \frac{T}{2}, \\ -1, & \frac{T}{2} \le \varsigma < T, \\ 0, & \text{otherwise}. \end{cases} \tag{14}$$

The family of HW functions was constructed by scaling and translating the mother wavelet. These operations adjust the wavelet's scaling and translation to generate a complete set of basis functions[37]:

$$\psi_i(\varsigma) = \begin{cases} 1, & \frac{\gamma T}{2^j} \le \varsigma < \frac{(\gamma+0.5)T}{2^j}, \\ -1, & \frac{(\gamma+0.5)T}{2^j} \le \varsigma < \frac{(\gamma+1)T}{2^j}, \\ 0, & \text{otherwise}, \end{cases} \tag{15}$$

where $i \in N^+$ and $j, \delta \in N$ indices i, j, and δ are interconnected through the relationships $i = 2^j + \gamma$, with constrained to the interval $0 \le \gamma < 2^j$. For further details on HW functional representations, see Ref.[38]

The HW system is characterized by orthogonal basis functions, which can be formally defined as39:

$$\int_0^1 \psi_i(\varsigma)\psi_{i'}(\varsigma)\, d\varsigma = \begin{cases} 1, & i = i', \\ 0, & i \ne i'. \end{cases} \tag{16}$$

Any$f(\varsigma) \in L^2[0,1)$ can be expressed in Haar series as follows[36]:

$$f(\varsigma) = \sum_{i=0}^{\infty} \vartheta_i \psi_i(\varsigma), \tag{17}$$

The function $f(\varsigma)$ can be approximated by truncating the series Equation (17) after the first terms, yielding:

$$f(\varsigma) \approx \sum_{i=0}^{p-1} \vartheta_i \psi_i(\varsigma) = \mathbf{C}_p \mathbf{\Psi}_p(\varsigma), \tag{18}$$

where $\mathbf{C}_p = [\vartheta_0,\ \vartheta_1, ...\vartheta_{p-1}]^T$, and $\mathbf{\Psi}_p(\varsigma) = [\psi_0(\varsigma),\ \psi_1(\varsigma), ..., \psi_{p-1}(\varsigma)]^T$.

Select p collocation points (CPs) across the interval $[0,T]$ to discretize the domain for numerical analysis $\varsigma_\varepsilon = \frac{2\varepsilon-1}{2p}T$, where $\varepsilon = 1, 2, ..., p, and p = 2^{\varpi+1}, \varpi = 0, 1, 2...$, and discretized Haar matrix $\mathbf{\Psi}_{p\times p}(\varsigma)$ as:

$$\mathbf{\Psi}_{p\times p}(\varsigma) = \begin{bmatrix} \psi_0\left(\frac{1}{2p}T\right) & \psi_0\left(\frac{3}{2p}T\right) & \cdots & \psi_0\left(\frac{2p-1}{2p}T\right) \\ \psi_1\left(\frac{1}{2p}T\right) & \psi_1\left(\frac{3}{2p}T\right) & \cdots & \psi_1\left(\frac{2p-1}{2p}T\right) \\ \vdots & \vdots & \ddots & \vdots \\ \psi_{m-1}\left(\frac{1}{2p}T\right) & \psi_{m-1}\left(\frac{3}{2p}T\right) & \cdots & \psi_{m-1}\left(\frac{2p-1}{2p}T\right) \end{bmatrix}. \tag{19}$$

4.2. Atangana–Baleanu fractional integral operational matrix

The Atagana–Baleanu fractional integral of order for the Haar scaling function and the HW is given as:

$${}_0^{AB}I_\varsigma^\varphi \mathbf{\Psi}_p(\varsigma) = F_{p\times p}^\varphi(\varsigma) =$$

$$\left[{}_0^{AB}I_\varsigma^\varphi \psi_0(\varsigma),\ {}_0^{AB}I_\varsigma^\varphi \psi_1(\varsigma), ...\ {}_0^{AB}I_\varsigma^\varphi \psi_{p-1}(\varsigma)\right]^T,$$

$$= \left[\frac{1-\varphi}{Q(\varphi)}\psi 0(\varsigma) + \frac{\varphi}{Q(\varphi)} 0 J_\varsigma^\varphi \psi 0(\varsigma),\ \frac{1-\varphi}{Q(\varphi)}\psi 1(t) + \frac{\varphi}{Q(\varphi)} 0 J\varsigma^\varphi \psi_1(\varsigma)\right.$$
$$\left., ..., \frac{1-\varphi}{Q(\varphi)}\psi p-1(\varsigma), + \frac{\varphi}{Q(\varphi)} 0 J_\varsigma^\varphi \psi_{p-1}(\varsigma)\right]^T$$

$$= [F\psi_0(\varsigma), F\psi_1(\varsigma), ..., F\psi_{p-1}(\varsigma)]^T,$$

where

$$F\psi_0(\varsigma) = \frac{1-\varphi}{Q(\varphi)} + \frac{\varsigma^\varphi}{Q(\varphi)\Gamma(\varphi)},\ 0 \le\ \varsigma < T, \tag{20}$$

and

$$F\psi_i(\varsigma) = \begin{cases} 0, & 0 \le \varsigma \frac{\gamma}{2^j} T, \\ g_1, & \frac{\gamma}{2^j} T \le \varsigma \frac{\gamma+0.5}{2^j} T, \\ g_2, & \frac{\gamma+0.5}{2^j} T \le \varsigma \frac{\gamma+1}{2^j} T, \\ g_3, & \frac{\gamma+1}{2^j} T \le \varsigma T. \end{cases} \tag{21}$$

where

$$g_1 = \frac{1-\varphi}{Q(\varphi)} + \frac{1}{Q(\varphi)\Gamma(\varphi)}\left(\varsigma - \frac{\gamma}{2^j}\right)^\varphi,$$

$$g_2 = \frac{1}{Q(\varphi)\Gamma(\varphi)}\left(\left(\varsigma - \frac{\gamma}{2^j}\right)^\varphi - 2\left(\varsigma - \frac{\gamma+\frac{1}{2}}{2^j}\right)^\varphi\right),$$

$$g_3 = \frac{1}{Q(\varphi)\Gamma(\varphi)}\left(\left(\varsigma - \frac{\gamma}{2^j}\right)^\varphi - 2\left(\varsigma - \frac{\gamma+\frac{1}{2}}{2^j}\right)^\varphi + \left(\varsigma - \frac{\gamma+1}{2^j}\right)^\varphi\right).$$

By substituting CPs in Equations (20) and (21), the fractional order integration matrix $F_{p\times p}^\varphi = F\psi_i(\varsigma_i)$ for the HW function can be derived as follows:

$$F^{\varphi}_{p\times p}=\begin{bmatrix} F\psi_0\left(\frac{1}{2p}T\right) & F\psi_0\left(\frac{3}{2p}T\right) & \cdots & F\psi_0\left(\frac{2p-1}{2p}T\right)\\ F\psi_1\left(\frac{1}{2p}T\right) & F\psi_1\left(\frac{3}{2p}T\right) & \cdots & F\psi_1\left(\frac{2p-1}{2p}T\right)\\ \vdots & \vdots & \ddots & \vdots\\ F\psi_p\left(\frac{1}{2p}T\right) & F\psi_p\left(\frac{3}{2p}T\right) & \cdots & F\psi_p\left(\frac{2p-1}{2p}T\right)\end{bmatrix}.$$

For convenience, $F^{\varphi}_{p\times p}(\varsigma)$ and $\mathbf{\Psi}_{p\times p}(\varsigma)$ can be written as $F^{\varphi}_{p\times p}$ and $\mathbf{\Psi}_{p\times p}$.

4.3. Implementation of the method for atmospheric model

This section details the computational procedure for solving the atmospheric model, where$E(\varsigma)=\sin(2\pi\varsigma)$. Consider Equation (1) as follows:

$$\begin{aligned}
{}^{ABC}_{0}D^{\varphi}_{\varsigma}f(\varsigma) =& -af(\varsigma)+bg(\varsigma)+\alpha_1\sin(2\pi\varsigma),\\
{}^{ABC}_{0}D^{\varphi}_{\varsigma}g(\varsigma) =& -\eta g(\varsigma)+\xi f(\varsigma)h(\varsigma)\\
&+\mu f^3(\varsigma)+\alpha_2\sin(2\pi\varsigma),\\
{}^{ABC}_{0}D^{\varphi}_{\varsigma}h(\varsigma) =& -\sigma h(\varsigma)+\lambda f(\varsigma)g(\varsigma)-\beta h^2(\varsigma)\\
&+\alpha_3\sin(2\pi\varsigma).
\end{aligned}\tag{22}$$

with initial conditions

$$f(0)=w_1,\ g(0)=w_2,\ h(0)=w_3.$$

The fractional-order derivatives in Equation (22) were numerically approximated by applying HW series expansion.

$$\begin{aligned}
{}^{ABC}_{0}D^{\varphi}_{\varsigma}f(\varsigma)&=\mathbf{C}^{(1)}_{p}\mathbf{\Psi}_{p\times p},\\
{}^{ABC}_{0}D^{\varphi}_{\varsigma}g(\varsigma)&=\mathbf{C}^{(2)}_{p}\mathbf{\Psi}_{p\times p},\\
{}^{ABC}_{0}D^{\varphi}_{\varsigma}h(\varsigma)&=\mathbf{C}^{(3)}_{p}\mathbf{\Psi}_{p\times p}.
\end{aligned}\tag{23}$$

By applying the Atangana–Baleanu fractional integral operator to Equation (23) and incorporating the initial conditions, we derive the following result:

$$\begin{aligned}
\left({}^{AB}_{0}I^{\varphi}_{\varsigma}\,{}^{ABC}_{0}D^{\varphi}_{\varsigma}f\right)(\varsigma)&=\mathbf{C}^{(1)}_{p}\left({}^{AB}_{0}I^{\varphi}_{\varsigma}\mathbf{\Psi}_{p\times p}\right),\\
\left({}^{AB}_{0}I^{\varphi}_{\varsigma}\,{}^{ABC}_{0}D^{\varphi}_{\varsigma}g\right)(\varsigma)&=\mathbf{C}^{(2)}_{p}\left({}^{AB}_{0}I^{\varphi}_{\varsigma}\mathbf{\Psi}_{p\times p}\right),\\
\left({}^{AB}_{0}I^{\varphi}_{\varsigma}\,{}^{ABC}_{0}D^{\varphi}_{\varsigma}h\right)(\varsigma)&=\mathbf{C}^{(3)}_{p}\left({}^{AB}_{0}I^{\varphi}_{\varsigma}\mathbf{\Psi}_{p\times p}\right).
\end{aligned}$$

$$\begin{aligned}
f(\varsigma)-f(0)&=\mathbf{C}^{(1)}_{p}F^{\varphi}_{p\times p},\\
g(\varsigma)-g(0)&=\mathbf{C}^{(2)}_{p}F^{\varphi}_{p\times p},\\
h(\varsigma)-h(0)&=\mathbf{C}^{(3)}_{p}F^{\varphi}_{p\times p}.
\end{aligned}$$

Using initial conditions, we obtain

$$\begin{aligned}
f(\varsigma)&=w_1+\mathbf{C}^{(1)}_{p}F^{\varphi}_{p\times p},\\
g(\varsigma)&=w_2+\mathbf{C}^{(2)}_{p}F^{\varphi}_{p\times p},\\
h(\varsigma)&=w_3+\mathbf{C}^{(3)}_{p}F^{\varphi}_{p\times p}.
\end{aligned}\tag{24}$$

By substituting Equations (23) and (24) into Equation (22), we derive the following result:

$$\begin{aligned}
\mathbf{C}^{(1)}_{p}\mathbf{\Psi}_{p\times p}=&-a\left(w_1+\mathbf{C}^{(1)}_{p}F^{\varphi}_{p\times p}\right)+b\left(w_2+\mathbf{C}^{(2)}_{p}F^{\varphi}_{p\times p}\right)\\
&+\alpha_1\sin(2\pi\varsigma),\\
\mathbf{C}^{(2)}_{p}\mathbf{\Psi}_{p\times p}=&-\eta\left(w_2+\mathbf{C}^{(2)}_{p}F^{\varphi}_{p\times p}\right)+\xi\left(w_1+\mathbf{C}^{(1)}_{p}F^{\varphi}_{p\times p}\right)\\
&\left(w_3+\mathbf{C}^{(3)}_{p}F^{\varphi}_{p\times p}\right)+\mu\left(w_1+\mathbf{C}^{(1)}_{p}F^{\varphi}_{p\times p}\right)^3\\
&+\alpha_2\sin(2\pi\varsigma),\\
\mathbf{C}^{(3)}_{p}\mathbf{\Psi}_{p\times p}=&-\sigma\left(w_3+\mathbf{C}^{(3)}_{p}F^{\varphi}_{p\times p}\right)+\lambda\left(w_1+\mathbf{C}^{(1)}_{p}F^{\varphi}_{p\times p}\right)\\
&\left(w_2+\mathbf{C}^{(2)}_{p}F^{\varphi}_{p\times p}\right)-\beta\left(w_3+\mathbf{C}^{(3)}_{p}F^{\varphi}_{p\times p}\right)^2\\
&+\alpha_3\sin(2\pi\varsigma).
\end{aligned}\tag{25}$$

We can write Equation (25) as

$$\begin{aligned}
A=&\mathbf{C}^{(1)}_{p}\mathbf{\Psi}_{p\times p}+a\left(w_1+\mathbf{C}^{(1)}_{p}F^{\varphi}_{p\times p}\right)-b\left(w_2+\mathbf{C}^{(2)}_{p}F^{\varphi}_{p\times p}\right)\\
&+\alpha_1\sin(2\pi\varsigma),\\
B=&\mathbf{C}^{(2)}_{p}\mathbf{\Psi}_{p\times p}+\eta\left(w_2+\mathbf{C}^{(2)}_{p}F^{\varphi}_{p\times p}\right)-\xi\left(w_1+\mathbf{C}^{(1)}_{p}F^{\varphi}_{p\times p}\right)\\
&\left(w_3+\mathbf{C}^{(3)}_{p}F^{\varphi}_{p\times p}\right)-\mu\left(w_1+\mathbf{C}^{(1)}_{p}F^{\varphi}_{p\times p}\right)^3\\
&+\alpha_2\sin(2\pi\varsigma),\\
S=&\mathbf{C}^{(3)}_{p}\mathbf{\Psi}_{p\times p}+\sigma\left(w_3+\mathbf{C}^{(3)}_{p}F^{\varphi}_{p\times p}\right)-\lambda\left(w_1+\mathbf{C}^{(1)}_{p}F^{\varphi}_{p\times p}\right)\\
&\left(w_2+\mathbf{C}^{(2)}_{p}F^{\varphi}_{p\times p}\right)+\beta\left(w_3+\mathbf{C}^{(3)}_{p}F^{\varphi}_{p\times p}\right)^2\\
&+\alpha_3\sin(2\pi\varsigma).
\end{aligned}\tag{26}$$

To resolve the system of algebraic equations given in Equation (26), the objective function is formulated as follows:

$$\Omega=\frac{1}{2p^2}\sum_{i=0}^{p-1}\left(A^2+B^2+S^2\right),\tag{27}$$

The unknown HW coefficients in Equation (27) are obtained using differential evolution optimization.

Example 1. Consider Equation (22) as

$$\begin{aligned}
{}^{ABC}_{0}D^{\varphi}_{\varsigma}f(\varsigma) =&1.8f(\varsigma)-1.8g(\varsigma)+0.01\sin(2\pi\varsigma),\\
{}^{ABC}_{0}D^{\varphi}_{\varsigma}g(\varsigma) =&-7.2g(\varsigma)+f(\varsigma)h(\varsigma)+0.02f^3\\
&(\varsigma)+0.01\sin(2\pi\varsigma),\\
{}^{ABC}_{0}D^{\varphi}_{\varsigma}h(\varsigma) =&-2.7h(\varsigma)+f(\varsigma)g(\varsigma)-0.07h^2\\
&(\varsigma)+0.01\sin(2\pi\varsigma).
\end{aligned}\tag{28}$$

with initial conditions

$$f(0)=1,\ g(0)=1,\ \text{and}\ h(0)=1,$$

Let

$$\begin{aligned}
{}^{ABC}_{0}D^{\varphi}_{\varsigma}f(\varsigma)&=\mathbf{C}^{(1)}_{p}\mathbf{\Psi}_{p\times p},\\
{}^{ABC}_{0}D^{\varphi}_{\varsigma}g(\varsigma)&=\mathbf{C}^{(2)}_{p}\mathbf{\Psi}_{p\times p},\\
{}^{ABC}_{0}D^{\varphi}_{\varsigma}h(\varsigma)&=\mathbf{C}^{(3)}_{p}\mathbf{\Psi}_{p\times p}.
\end{aligned}\tag{29}$$

By applying the Atangana–Baleanu fractional integral operator to Equation (29) and incorporating the initial conditions, we derive the following result:

$$\begin{aligned}
\left({}_0^{AB}I_\varsigma^\varphi\, {}_0^{ABC}D_\varsigma^\varphi f\right)(\varsigma) &= \mathbf{C}_p^{(1)}\left({}_0^{AB}I_\varsigma^\varphi \mathbf{\Psi}_{p\times p}\right),\\
\left({}_0^{AB}I_\varsigma^\varphi\, {}_0^{ABC}D_\varsigma^\varphi g\right)(\varsigma) &= \mathbf{C}_p^{(2)}\left({}_0^{AB}I_\varsigma^\varphi \mathbf{\Psi}_{p\times p}\right),\\
\left({}_0^{AB}I_\varsigma^\varphi\, {}_0^{ABC}D_\varsigma^\varphi h\right)(\varsigma) &= \mathbf{C}_p^{(3)}\left({}_0^{AB}I_\varsigma^\varphi \mathbf{\Psi}_{p\times p}\right).
\end{aligned}$$

$$\begin{aligned}
f(\varsigma) - f(0) &= \mathbf{C}_p^{(1)} F_{p\times p}^\varphi,\\
g(\varsigma) - g(0) &= \mathbf{C}_p^{(2)} F_{p\times p}^\varphi,\\
h(\varsigma) - h(0) &= \mathbf{C}_p^{(3)} F_{p\times p}^\varphi.
\end{aligned}$$

Using initial conditions, we obtain

$$\begin{aligned}
f(\varsigma) &= 1 + \mathbf{C}_p^{(1)} F_{p\times p}^\varphi,\\
g(\varsigma) &= 1 + \mathbf{C}_p^{(2)} F_{p\times p}^\varphi,\\
h(\varsigma) &= 1 + \mathbf{C}_p^{(3)} F_{p\times p}^\varphi.
\end{aligned} \tag{30}$$

By substituting Equations (29) and (30) into Equation (28), we derive the following result:

$$\begin{aligned}
\mathbf{C}_p^{(1)}\mathbf{\Psi}_{p\times p} =& 1.8\left(1 + \mathbf{C}_p^{(1)} F_{p\times p}^\varphi\right) - 1.8\\
&\left(1 + \mathbf{C}_p^{(2)} F_{p\times p}^\varphi\right) + 0.01\sin(2\pi\varsigma),\\
\mathbf{C}_p^{(2)}\mathbf{\Psi}_{p\times p} =& -7.2\left(1 + \mathbf{C}_p^{(2)} F_{p\times p}^\varphi\right)\\
&+ \left(1 + \mathbf{C}_p^{(1)} F_{p\times p}^\varphi\right)\left(1 + \mathbf{C}_p^{(3)} F_{p\times p}^\varphi\right)\\
&+ 0.02\left(1 + \mathbf{C}_p^{(1)} F_{p\times p}^\varphi\right)^3\\
&+ 0.01\sin(2\pi\varsigma),\\
\mathbf{C}_p^{(3)}\mathbf{\Psi}_{p\times p} =& -2.7\left(1 + \mathbf{C}_p^{(3)} F_{p\times p}^\varphi\right)\\
&+ \left(1 + \mathbf{C}_p^{(1)} F_{p\times p}^\varphi\right)\left(1 + \mathbf{C}_p^{(2)} F_{p\times p}^\varphi\right)\\
&- 0.07\left(1 + \mathbf{C}_p^{(3)} F_{p\times p}^\varphi\right)^2\\
&+ 0.01\sin(2\pi\varsigma).
\end{aligned} \tag{31}$$

We can write Equation (31) as

$$\begin{aligned}
A_1 =& \mathbf{C}_p^{(1)}\mathbf{\Psi}_{p\times p}\\
&- 1.8\left(1 + \mathbf{C}_p^{(1)} F_{p\times p}^\varphi\right)\\
&+ 1.8\left(1 + \mathbf{C}_p^{(2)} F_{p\times p}^\varphi\right) - \mathbf{E},\\
B_1 =& \mathbf{C}_p^{(2)}\mathbf{\Psi}_{p\times p}\\
&+ 7.2\left(w_2 + \mathbf{C}_p^{(2)} F_{p\times p}^\varphi\right) - \left(1 + \mathbf{C}_p^{(1)} F_{p\times p}^\varphi\right)\\
&\left(1 + \mathbf{C}_p^{(3)} F_{p\times p}^\varphi\right)\\
&- 0.02\left(1 + \mathbf{C}_p^{(1)} F_{p\times p}^\varphi\right)^3 - \mathbf{E},\\
C_1 =& \mathbf{C}_p^{(3)}\mathbf{\Psi}_{p\times p}\\
&+ 2.7\left(1 + \mathbf{C}_p^{(3)} F_{p\times p}^\varphi\right)\\
&+ \left(w_1 + \mathbf{C}_p^{(1)} F_{p\times p}^\varphi\right)\left(1 + \mathbf{C}_p^{(2)} F_{p\times p}^\varphi\right)\\
&+ 0.07\left(1 + \mathbf{C}_p^{(3)} F_{p\times p}^\varphi\right)^2 - \mathbf{E}.
\end{aligned} \tag{32}$$

where

$$\mathbf{E} = \begin{bmatrix}
0.01\sin(2\pi\varsigma_1) & 0 & 0 & 0\\
0 & 0.01\sin(2\pi\varsigma_2) & 0 & 0\\
\vdots & 0 & \ddots & 0\\
0 & 0 & 0 & 0.01\sin(2\pi\varsigma_{2p})
\end{bmatrix}$$

To resolve the system of algebraic equations in Equation (32), the objective function is formulated as follows:

$$\Omega_1 = \frac{1}{2p^2}\sum_{i=0}^{p-1}\left(A_1^2 + B_1^2 + S_1^2\right), \tag{33}$$

The unknown HW coefficients in Equation (33) are obtained using differential evolution optimization.

4.4. Differential evolution algorithm

The heuristic optimization technique outlined by Storn[40] is highly effective. Differential evolution is widely used among global optimizers owing to its simplicity and powerful population-based stochastic search approach for continuous domains. The algorithm is defined by three key control parameters: scaling factor Sf, crossover constant CR, and population size NP. These factors significantly influence the performance of DE optimization. Thus, in Ref.[40], several straightforward criteria are provided for selecting these values. In the DE algorithm, solutions can be derived by providing the population set, an approximation solution, and the objective function.

4.5. Error and convergence analysis

This section presents the derivation of inequality pertaining to the upper bound of the ABC operator. The proof follows a methodology similar to that detailed in Ref.[41]. For the convergence analysis of the HWOMM, we hypothesize the existence of a continuous and bounded function $f^n(\varsigma)$ on the interval $[0,1]$.

Theorem 2 Assume that ${}_0^{ABC}D_\varsigma^\varphi f(\varsigma) \in L^2[0,1)$ and $p = 2^{\varpi+1}$. Let $f(t)$ denotes exact solutions of system (1), and $\bar{f}(\varsigma)$ represent the approximate solutions obtained using HWOMM. The derivative $f^n(\varsigma)$ is continuous, and $\exists\, K > 0,\ \forall\, \varsigma \in [0,1),\ |f^n(\varsigma)| \le K$. Under these assumptions, the exact upper bound for the ABC derivative is as follows:

$$\left\|{}_0^{ABC}D_\varsigma^\varphi f(\varsigma) - {}_0^{ABC}D_\varsigma^\varphi \bar{f}(\varsigma)\right\|_E \le \frac{KQ(\varphi)}{(1-\varphi)}\sum_{\hbar=0}^{\infty}\left(-\frac{\varphi}{1-\varphi}\right)^{\hbar} \frac{1}{\Gamma(\hbar\varphi+1)(\hbar\varphi+1)}\frac{1}{\left(2^{2(\hbar\varphi+1)}-1\right)^{\frac{1}{2}}}\frac{1}{p^{(\hbar\varphi+1)}}. \tag{34}$$

where ${}_0^{ABC}D_\varsigma^\varphi f(\varsigma) = \sum_{i=0}^{\infty}\vartheta_i\psi_i(\varsigma)$ and first p terms are ${}_0^{ABC}D_\varsigma^\varphi \bar{f}(\varsigma) = \sum_{i=0}^{p-1}\vartheta_i\psi_i(\varsigma)$, $\|f(\varsigma)\|_E = \left(\int_0^1 f^2(\varsigma)\,d\varsigma\right)^{\frac{1}{2}}$.

Proof For complete proof, see Ref.[42]

Theorem 3 If $f(\varsigma)$ is continuous, $p = 2^{\varpi+1}$, and $\exists\, K > 0$, such that $|f^n(\varsigma)| \le K$. Then we have

$$\left\|f(\varsigma) - \bar{f}(\varsigma)\right\|_E \le K\sum_{\hbar=0}^{\infty}\left(-\frac{\varphi}{1-\varphi}\right)^{\hbar} \frac{1}{\Gamma(\hbar\varphi+1)(\hbar\varphi+1)}\frac{1}{\left(2^{2(\hbar\varphi+1)}-1\right)}\frac{1}{p^{2(\hbar\varphi+1)}} + \frac{K\,T^\varphi}{Q(\varphi)\Gamma(\varphi)}\sum_{\hbar=0}^{\infty}\left(-\frac{\varphi}{1-\varphi}\right)^{\hbar}\frac{1}{\Gamma(\hbar\varphi+1)(\hbar\varphi+1)} \frac{1}{\left(2^{2(\hbar\varphi+1)}-1\right)^{\frac{1}{2}}}\frac{1}{p^{(\hbar\theta+1)}}. \tag{35}$$

This implies that $\left\|f(\varsigma) - \bar{f}(\varsigma)\right\|_E \to 0$ when $p \to \infty$.

Proof The following can be easily derived from Lemma 1 and Equation (35):

$$\begin{aligned}\left\|f(\varsigma) - \bar{f}(\varsigma)\right\|_E &= \left\|I^\varphi\,{}_0^{ABC}D_\varsigma^\varphi f(\varsigma) - I^\theta\,{}_0^{ABC}D_\varsigma^\varphi \bar{f}(\varsigma)\right\|_E \\ &= \left\|I^\varphi\left({}_0^{ABC}D_\varsigma^\varphi f(\varsigma) - {}_0^{ABC}D_\varsigma^\varphi \bar{f}(\varsigma)\right)\right\|_E \\ &= \left\|\frac{1-\varphi}{Q(\varphi)}\begin{pmatrix}\frac{\mathrm{K}\,Q(\varphi)}{(1-\varphi)}\\ \sum_{\mathrm{h}=0}^{\infty}\left(-\frac{\varphi}{1-\varphi}\right)^{\mathrm{h}}\frac{1}{\Gamma(\mathrm{h}\varphi+1)(\mathrm{h}\varphi+1)}\\ \frac{1}{\left(2^{2(\mathrm{h}\varphi+1)}-1\right)^{\frac{1}{2}}}\frac{1}{p^{(\mathrm{h}\varphi+1)}}\end{pmatrix}\right. \\ &\quad + \frac{\varphi}{Q(\varphi)\Gamma(\varphi)}\int_0^{\varsigma}(\varsigma-\tau)^{\eta-1} \left.\begin{pmatrix}\frac{\mathrm{K}\,Q(\varphi)}{(1-\varphi)}\sum_{\mathrm{h}=0}^{\infty}\left(-\frac{\varphi}{1-\varphi}\right)^{\mathrm{h}}\frac{1}{\Gamma(\mathrm{h}\varphi+1)(\mathrm{h}\varphi+1)}\\ \frac{1}{\left(2^{2(\mathrm{h}\varphi+1)}-1\right)^{\frac{1}{2}}}\frac{1}{p^{(\mathrm{h}\varphi+1)}}\end{pmatrix}d\tau\right\|_E, \\ &= \left\|\mathrm{K}\sum_{\mathrm{h}=0}^{\infty}\left(-\frac{\varphi}{1-\varphi}\right)^{\mathrm{h}}\frac{1}{\Gamma(\mathrm{h}\varphi+1)(\mathrm{h}\varphi+1)} \frac{1}{\left(2^{2(\mathrm{h}\varphi+1)}-1\right)^{\frac{1}{2}}}\frac{1}{p^{(\mathrm{h}\varphi+1)}}\right. \\ &\quad \left.+\frac{\varphi\mathrm{K}}{Q(\varphi)\Gamma(\varphi)}\sum_{\mathrm{h}=0}^{\infty}\left(-\frac{\varphi}{1-\varphi}\right)^{\mathrm{h}}\frac{1}{\Gamma(\mathrm{h}\varphi+1)(\mathrm{h}\varphi+1)} \frac{1}{\left(2^{2(\mathrm{h}\varphi+1)}-1\right)^{\frac{1}{2}}}\frac{1}{p^{(\mathrm{h}\varphi+1)}}\frac{\varsigma^\varphi}{\varphi}\right\|_E, \\ &\le K\sum_{k=0}^{\infty}\left(-\frac{\varphi}{1-\varphi}\right)^{k}\frac{1}{\Gamma(\hbar\varphi+1)(\hbar\varphi+1)} \frac{1}{\left(2^{2(\hbar\varphi+1)}-1\right)^{\frac{1}{2}}}\frac{1}{p^{(\hbar\varphi+1)}} \\ &\quad + \frac{K\,T^\varphi}{Q(\varphi)\Gamma(\varphi)}\sum_{\hbar=0}^{\infty}\left(-\frac{\varphi}{1-\varphi}\right)^{\hbar}\frac{1}{\Gamma(\hbar\varphi+1)(\hbar\varphi+1)} \frac{1}{\left(2^{2(\hbar\varphi+1)}-1\right)^{\frac{1}{2}}}\frac{1}{p^{(\hbar\varphi+1)}}.\end{aligned}$$

This confirms the desired result.

Theorem 3 presents an inequality that depends on known parameters K, T, $Q(\varphi)$, $\Gamma(k\varphi+1)$ and φ with p as the sole variable parameter. As a result, the upper bound of the error is determined based on p. Specifically, as p increases, the upper bound of the error decreases, leading to a smaller computed error. From this observation, we conclude

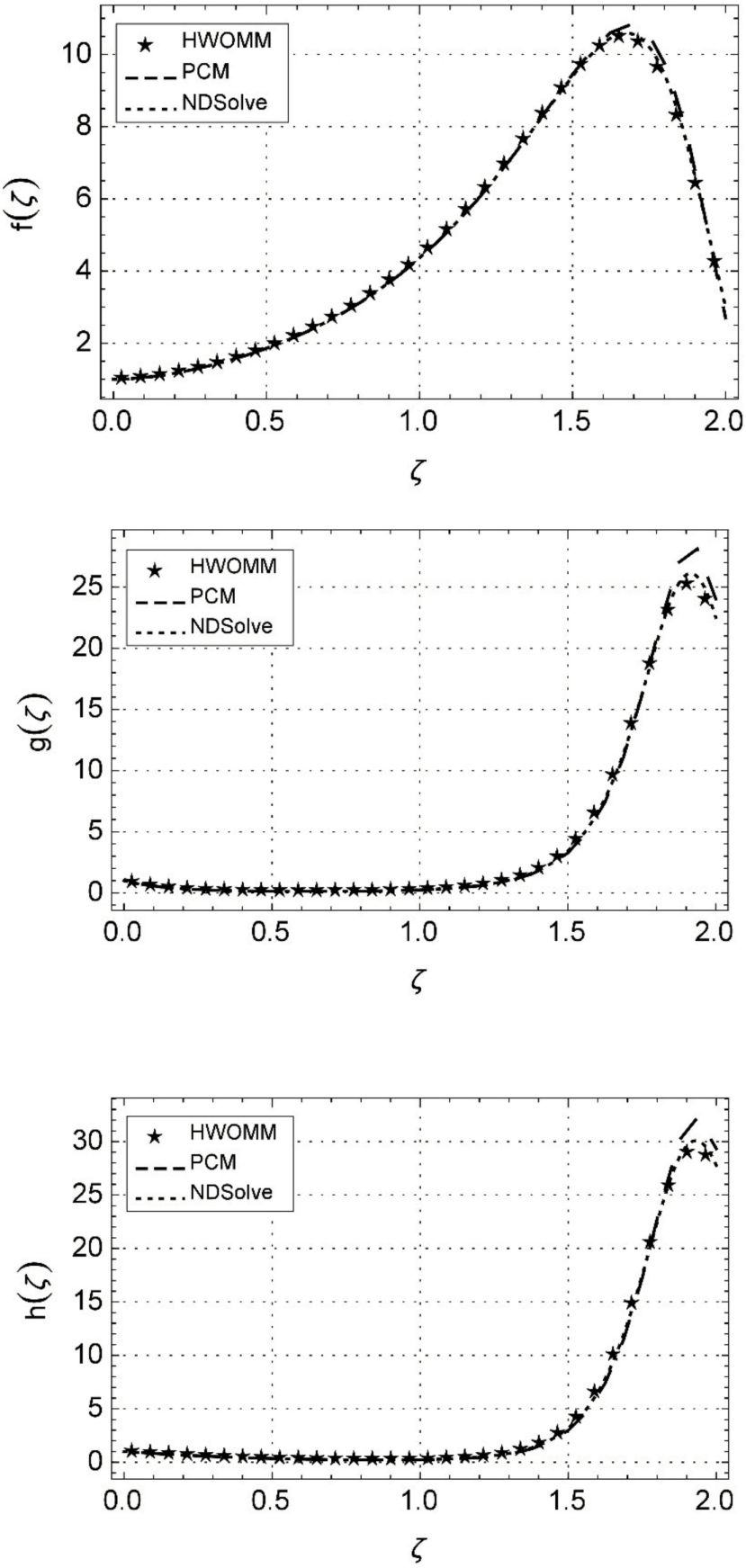

Figure 1. Comparison of the Haar wavelet operational matrix method (HWOMM) with the predictor–corrector method (PCM)[33] and numerical results for atmospheric components $f(\varsigma)$, $g(\varsigma)$ and $h(\varsigma)$ at $\varphi = 1, p = 32$, and time $\varsigma = 2$ days

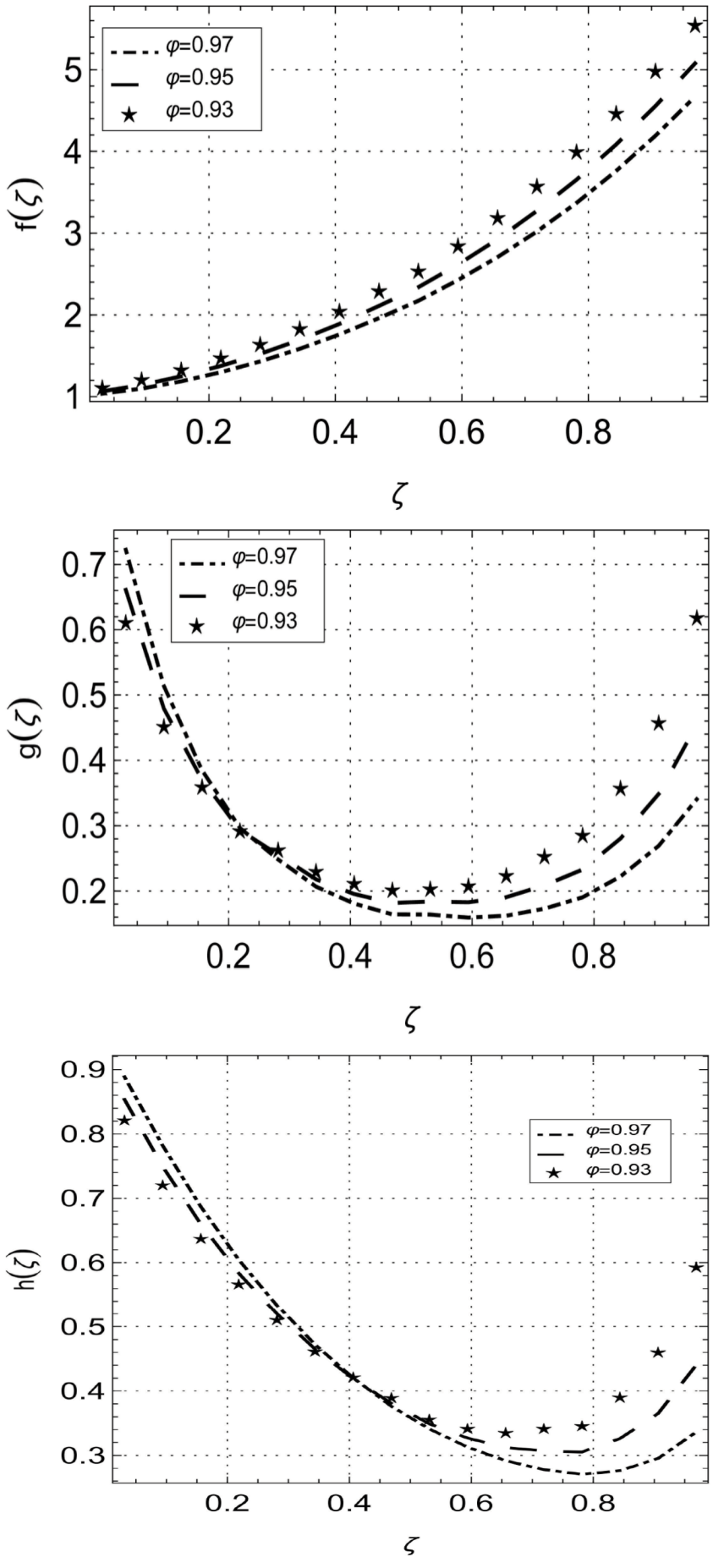

Figure 2. Solution of atmospheric components $f(\varsigma)$, $g(\varsigma)$, and $h(\varsigma)$ using the Haar wavelet operational matrix method different fractional orders for $p = 16$ and $\varsigma = 1$

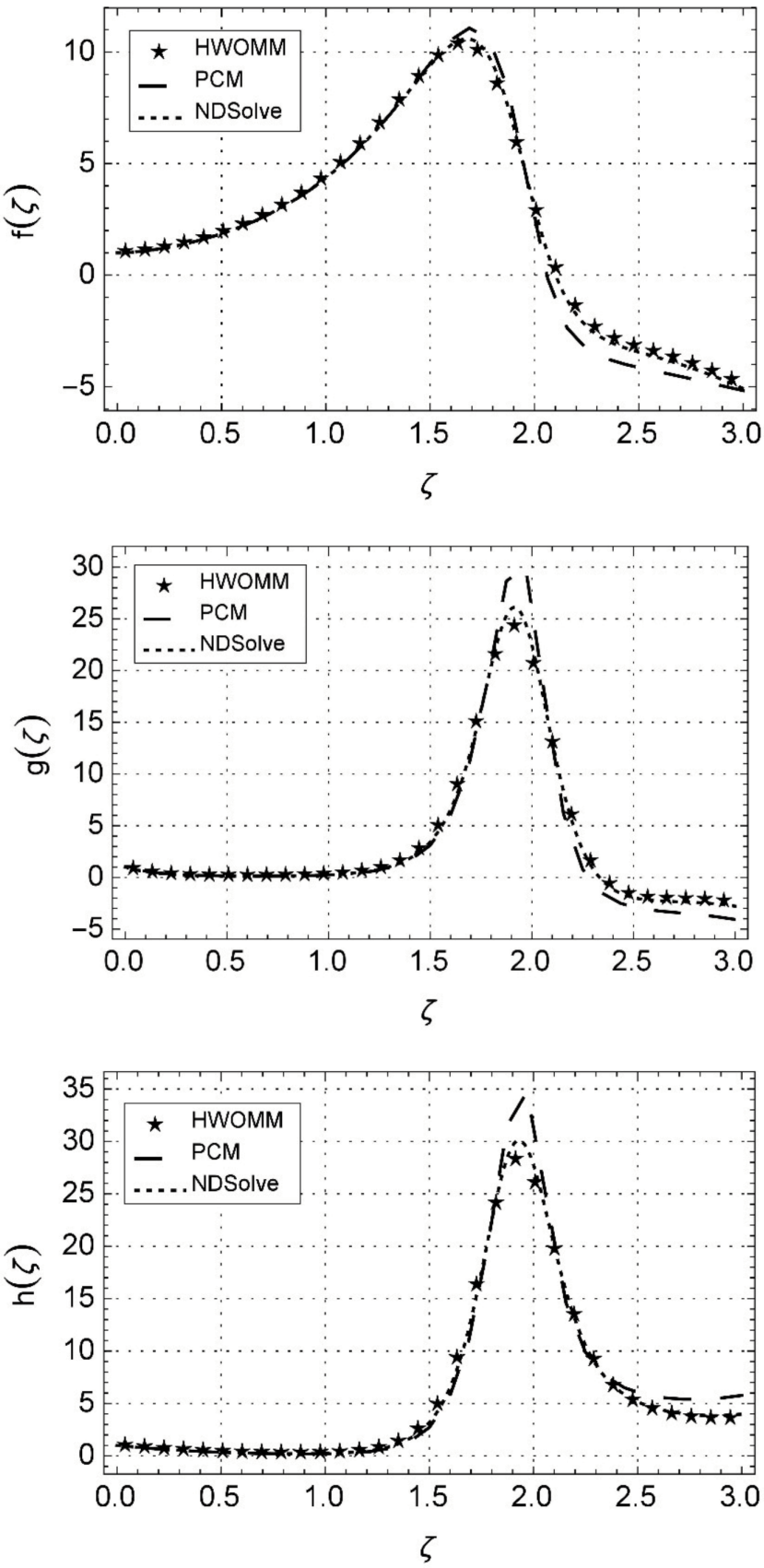

Figure 3. Comparison of the Haar wavelet operational matrix method with the predictor–corrector method[33] and numerical results for atmospheric components $f(\varsigma)$, $g(\varsigma)$, and $h(\varsigma)$ at $\varphi = 1, p = 32$, and time $\varsigma = 3$ days

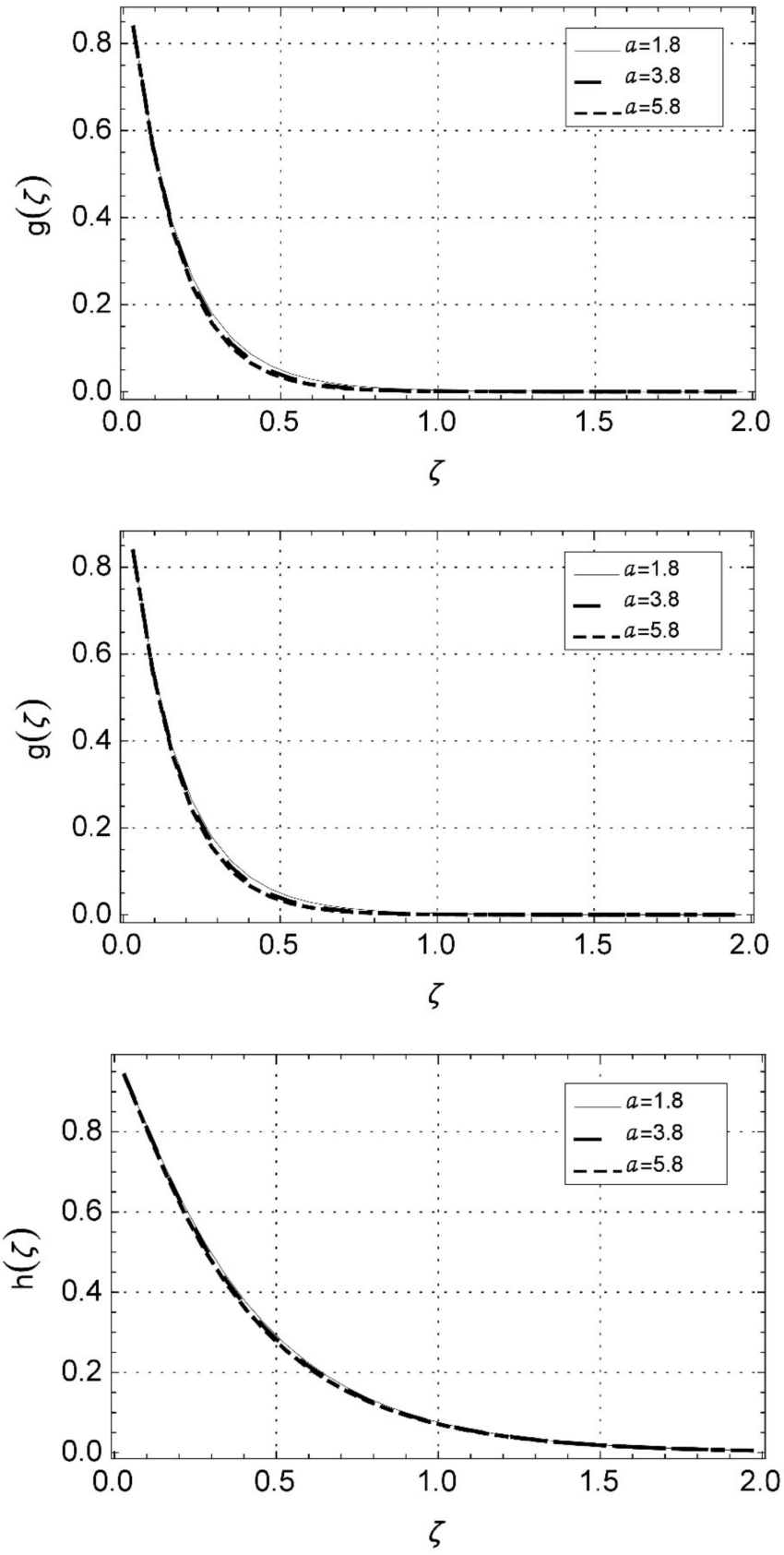

Figure 4. Graphical illustration of the variation in water freezing rate and the resulting of permafrost (a) formation

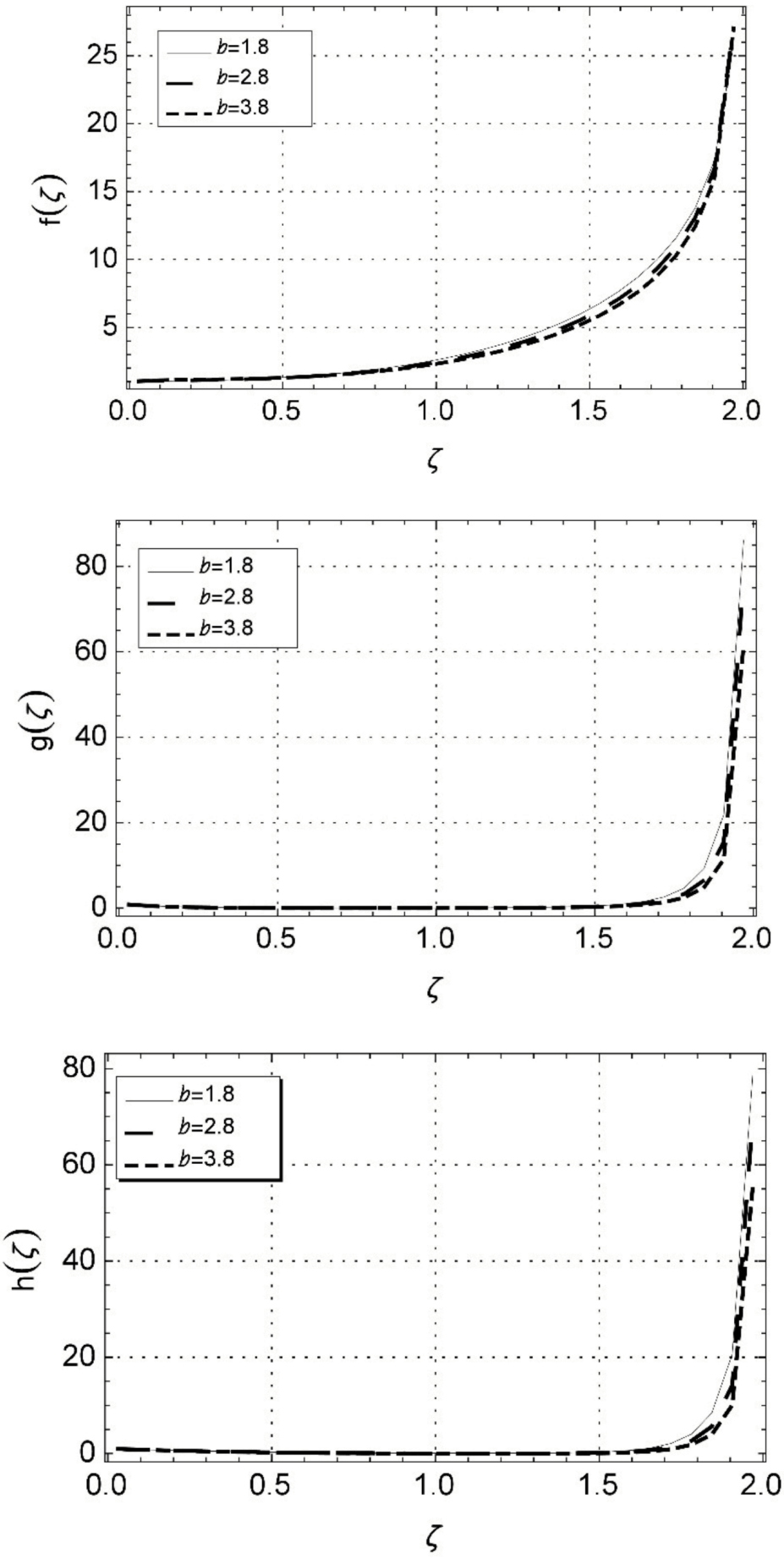

Figure 5. Graphical illustration of the variation in the rate of permafrost thaw and collapse (b)

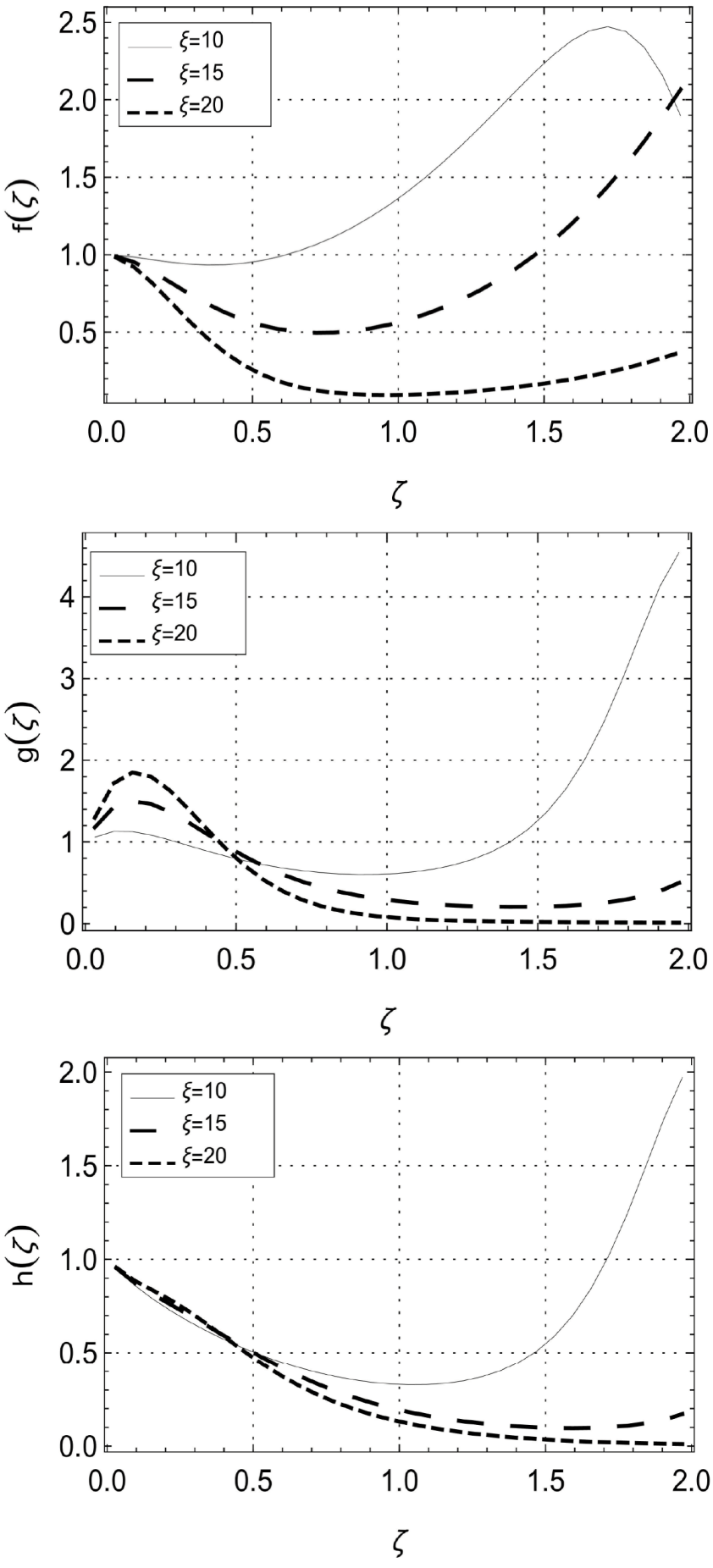

Figure 6. Graphical illustration of the variation in the temperature growth rate coefficient (ξ)

Table 1. Comparison of the Haar wavelet operational matrix method (HWOMM) with the predictor–corrector method (PCM)[33] for thawing permafrost $f(\varsigma)$, atmospheric temperature $g(\varsigma)$, and greenhouse gases $h(\varsigma)$ at $\varphi = 0.99$ at

ς	f_{HWOMM}	f_{PCM}	g_{HWOMM}	g_{PCM}	h_{HWOMM}	h_{PCM}
0	1.0167	1.0266	0.7973	0.7054	0.9258	0.8834
0.2	1.2314	1.2619	0.3003	0.2728	0.6285	0.5939
0.4	1.6473	1.6910	0.1651	0.1530	0.4236	0.3961
0.5	2.2583	2.3186	0.1351	0.1265	0.2991	0.2753
0.7	3.1210	3.1987	0.1545	0.1500	0.2392	0.2171
0.9	4.3123	4.4093	0.2575	0.2544	0.2608	0.2366
1.1	6.0291	6.0297	0.5317	0.5814	0.3822	0.4485
1.3	8.0889	8.0608	1.6162	1.6368	1.3384	1.3693
1.5	10.1585	10.0962	5.8277	5.3312	5.7517	5.1985
1.7	9.6666	10.1541	17.7634	16.9436	19.4748	18.3494
1.9	2.3773	2.4100	18.664	21.0066	24.2421	26.5627

Table 2. Comparison of the Haar wavelet operational matrix method (HWOMM) with the predictor–corrector method (PCM)[33] for thawing permafrost $f(\varsigma)$, atmospheric temperature $g(\varsigma)$, and greenhouse gases $h(\varsigma)$ at $\varphi = 0.97$

ς	f_{HWOMM}	f_{PCM}	g_{HWOMM}	g_{PCM}	h_{HWOMM}	h_{PCM}
0	1.0369	1.0377	0.7224	0.7253	0. 8887	0. 8758
0.2	1.2989	1.2803	0.2964	0.2679	0.6044	0.5897
0.4	1.7606	1.7258	0.1807	0.1552	0.4202	0.3964
0.5	2.4350	2.3742	0.1592	0.1345	0.3129	0.2817
0.7	3.3688	3.2812	0.1904	0.1651	0.2705	0.2311
0.9	4.6709	4.5250	0.3403	0.2868	0.3362	0.2670
1.1	6.7621	6.1771	0.8277	0.6677	0.6252	0.5334
1.3	8.9209	8.1985	2.6892	1.9152	3.9962	2.5881
1.5	10.0874	10.0141	11.4057	6.2856	17.2382	14.5080
1.7	6.5764	9.2540	20.8604	18.0806	23.7243	25.4811
1.9	0.8064	2.1521	8.7632	16.3396	14.6575	22.0811

Table 3. Root mean square error (RMSE), Nash–Sutcliffe efficiency (NSE), and convergence rate for the atmospheric model

ρ	E_{RMSE}			E_{NSE}			R_c			CPU time
	f	g	h	f	g	h	f	g	h	(s)
4	9.369×10^2	5.507×10^2	1.769×10^2	1.013×10^2	1.465×10^1	6.429×10^2	–	–	–	0.765
8	2.324×10^2	1.599×10^2	4.542×10^3	5.814×10^4	7.939×10^3	3.928×10^4	1.859	1.251	1.544	0.812
16	5.801×10^3	4.170×10^3	1.150×10^3	3.560×10^5	4.801×10^4	2.478 105	1.924	1.567	2.002	3.246
32	1.449 103	1.054 103	2.888 104	2.213 106	2.977 105	1.555 105	1.962	1.764	1.865	7.769
64	3.733 103	4.318 103	7.801 104	1.380 107	1.857 106	9.727 106	1.981	1.876	1.918	12.96

that:

$$\lim_{p\to\infty} \left\| f(\varsigma) - \bar{f}(\varsigma) \right\|_E = 0.$$

4.6. Performance measures

To evaluate the performance of HWOMM, the performance measures RMSE, ENSE, and the rate of convergence are mathematically defined as:

$$\mathrm{RMSE} = \sqrt{\frac{1}{2p}\sum_{i=0}^{p-1}\left(f_{i,HWOMM} - \bar{f}_{i,NDSolve}\right)^2}, \tag{36}$$

$$\mathrm{NSE} = 1 - \left(\frac{\sum_{i=0}^{p-1}\left(f_{i,HWOMM} - \bar{f}_{i,NDSolve}\right)^2}{\sum_{i=0}^{p-1}\left(f_{i,HWOMM}\right) - \frac{1}{p}\sum_{i=0}^{p-1}\left(f_{i,HWOMM}\right)^2}\right),$$
$$ENSE = |1 - NSE|. \tag{37}$$

$$R_c(p) = \frac{\log\left(\frac{E\left(\frac{p}{2}\right)}{E(p)}\right)}{\log(2)}. \tag{38}$$

where $f_{i,HWOMM}$ and $\bar{f}_{i,HWOMM}$ represent HWOMM solution and numerical solution, respectively, p denotes the number of CPs.

5. Results and discussion

The nonlinear atmospheric model described in Equation (1) was numerically investigated using HWOMM. In the absence of analytical solutions, the HWOMM outcomes were benchmarked against those derived using the NDSolve and PCM.[33] Figure 1 provides a comparative graphical representation of the results obtained using HWOMM, PCM,[33] and NDSolve, clearly demonstrating that the proposed HWOMM maintains close agreement with both reference methods. Figure 2 explores the dynamic behavior of each model component across different fractional order values $\varphi = 0.97$, 0.95, and 0.93. Notably, as the fractional order decreases, the response of permafrost compartment becomes more pronounced, particularly around $\varsigma = 1$. This behavior suggests that the atmospheric system is highly sensitive to variations in the fractional order. Because permafrost thawing releases greenhouse gases, this increased thaw leads to further atmospheric warming and accelerates the degradation of permafrost layers. Figure 3 presents a direct comparison between the results obtained by HWOMM and those obtained using PCM and NDSolve at $\varphi = 1$, and $\varsigma = 3$ days, showing that the proposed HWOMM achieves close agreement with benchmark methods, thereby confirming the accuracy and reliability of the method. Additionally, the results in Tables 1 and 2 clearly exhibit that HWOMM maintains stability across different fractional orders $\varphi = 0.99$ and 0.97, for $\varsigma = 2$ days, whereas PCM becomes unstable or diverges as the fractional order decreases. Moreover, the quantitative comparison highlights HWOMM superior accuracy and consistency. Figures 4–6 further delve into the impact of varying model parameters. Figure 4 depicts that increasing the rate at which water freezes and forms permafrost a leads to a simultaneous decrease in permafrost thawing $f(\varsigma)$, atmospheric temperature$g(\varsigma)$, and greenhouse gas concentration $h(\varsigma)$, implying a stabilizing effect on the environment. Figure 5 shows that an increase in the rate of permafrost thaw and collapse contributes to higher levels of permafrost thaw, elevated atmospheric temperature, and increased greenhouse gas emissions, thereby reinforcing the feedback loop derives climate change. Figure 6 illustrates the influence of the temperature growth coefficient ξ. Initially, higher values of this parameter cause permafrost thaw to decrease $f(\varsigma)$ while atmospheric temperature $g(\varsigma)$ and the greenhouse gases $h(\varsigma)$ level rise. However, after a certain threshold, all three components began to decrease, suggesting a nonlinear feedback mechanism. Finally, Table 3 presents performance metrics, the convergence rate, and computation central processing unit time in seconds.

6. Conclusion

In this work, we studied a fractional-order atmospheric model that simultaneously incorporates temperature, greenhouse gas concentration, and permafrost thaw, formulated using the ABC fractional derivative to capture memory and hereditary effects in climate dynamics. To efficiently solve the resulting nonlinear system, we developed an operational matrix for the ABC fractional integral operator based on HW.

The theoretical framework of the proposed method was established by proving the existence and uniqueness of the solution under suitable Lipschitz conditions. Numerical experiments were conducted and validated through comparisons with the PCM and numerical solutions obtained using NDSolve. The results confirmed that HWOMM yields highly accurate solutions with faster convergence and reduced computational cost. Error analysis demonstrated that the approximation error decreases with higher resolution levels, confirming the convergence of the method. Finally, performance metrics, including RMSE, ENSE, and convergence rate, further validated the robustness and precision of the proposed method. The HWOMM exhibited strong adaptability across different parameter values and fractional orders, making it a promising and computationally efficient tool for modeling complex atmospheric and environmental phenomena.

Nonetheless, the HWOMM has some intrinsic limitations. Given HWS are piecewise constant,

the method may require higher resolution levels to accurately capture steep gradients or highly oscillatory behaviors, which can increase computational effort. Future work will focus on extending the method to other fractional operators, higher dimensional partial differential equations, and hybrid optimization strategies to further enhance scalability, convergence speed, and applicability to more complex climate systems.

Acknowledgments

None.

Funding

None.

Conflict of interest

The authors declare that they have no known competing financial interests or personal relationships that could have appeared to influence the work reported in this paper.

Author contributions

Conceptualization: Mumtaz Ali, Najeeb Alam Khan, Nadeem Alam Khan
Formal analysis: Mumtaz Ali, Najeeb Alam Khan, Muhammad Ayaz
Methodology: Najeeb Alam Khan, Muhammad Ayaz
Software: Mumtaz Ali
Writing – original draft: Mumtaz Ali
Writing – review & editing: Najeeb Alam Khan, Nadeem Alam Khan

Availability of data

Not applicable.

AI tools statement

All authors confirm that no AI tools were used in the preparation of this manuscript.

References

1. Kilbas AA, Srivastava HM, Trujillo JJ. Theory and Applications of Fractional Differential Equations. *Elsevier*, Vol. 204. 2006, 1-523. https://doi.org/10.1016/S0304-0208(06)80001-0
2. Matlob MA, Jamali Y. The concepts and applications of fractional order differential calculus in modeling of viscoelastic systems: a primer. *Crit Rev Biomed Eng.* 2019;47(4):249-276. doi: 10.1615/CritRevBiomedEng.2018028368
3. Iqbal MAB, Raza MZ, Khan A, Abdeljawad T, Almutairi DK. Advanced wave dynamics in the STF-mBBM equation using fractional calculus. *Sci Rep.* 2025;15(1):5803. doi: 10.1038/s41598-025-90044-w
4. Öztürk Z, Yousuf A, Bilgil H, Sorgun S. A fractional-order mathematical model to analyze the stability and develop a sterilization strategy for the habitat of stray dogs. *Int J Optim Control Theory Appl.* 2024;14(2):134-146. doi:10.11121/ijocta.1418
5. Das A, Bhat R, Jolly MK. A Systems Biology View of Breast Cancer via Fractal Geometry and Fractional Calculus. 2025. doi:10.48550/arXiv.2505.07338
6. Ayaz F, Heredag K. Fractional model for blood flow under MHD influence in porous and non-porous media. *Int J Optim Control Theory Appl.* 2024;14(2):156-167. doi: 10.11121/ijocta.1497
7. Chen Q, Sabir Z, Raja MAZ, Gao W, Baskonus HM. A fractional study based on the economic and environmental mathematical model. *Alex Eng J.* 2023;65(1):761-770. doi:10.1016/j.aej.2022.09.033
8. Cheow YH, Ng KH, Phang C, Ng KH. The application of fractional calculus in economic growth modelling: an approach based on regression analysis. *Heliyon.* 2024;10(15):e35379. doi: 10.1016/j.heliyon.2024.e35379
9. Arora S, Mathur T, Agarwal S, Tiwari K, Gupta P. Applications of fractional calculus in computer vision: a survey. *Neurocomputing.* 2022;489:407-428. doi: 10.1016/j.neucom.2021.10.122
10. Kumar D, Baleanu D. Fractional calculus and its applications in physics. *Front Phys.* 2019;7(81):2. doi: 10.3389/fphy.2019.00081
11. Atangana A, Baleanu D. New fractional derivatives with nonlocal and non-singular kernel: Theory and application to heat transfer model. *Therm Sci.* 2016;20(2):763-769. doi: 10.2298/TSCI160111018A
12. Deressa CT. On the chaotic nature of the Rabinovich system through Caputo and Atangana–Baleanu–Caputo fractional derivatives. *Adv Contin Discrete Models.* 2022;66(2022). doi: 10.1186/s13662-022-03740-6
13. Shaikh A, Qureshi S. Comparative analysis of riemann-liouville, Caputo-Fabrizio, and Atangana-Baleanu integrals. *J Appl Math Comput Mech.* 2022;21(1):91-101. doi: 10.17512/jamcm.2022.1.08
14. Kneisel C, Hauk C, Fortier R, Moorman B. Advances in geophysical methods for permafrost investigations. *Permafr Periglac Process.* 200;19(2):157-178. doi: 10.1002/ppp.616
15. Obu J. How much of the Earth's surface is underlain by permafrost? *J Geophys Res Earth Surf.*

2021;126(5):e2021JF006123.
doi: 10.1029/2021JF006123

16. Wu Q, Zhang T. Changes in active layer thickness over the Qinghai-Tibetan Plateau from 1995 to 2007. *J Geophys Res Atmos.* 2010;115(D9).
doi: 10.1029/2009JD012974
17. Harp DR, Atchley AL, Painter SL, et al. Effect of soil property uncertainties on permafrost thaw projections: a calibration-constrained analysis. *Cryosphere.* 2016;10(1):341-358.
https://doi.org/10.5194/tc-10-341-2016
18. Pan Y, Li L, Jiang X, et al. Earth's changing global atmospheric energy cycle in response to climate change. *Nat Commun.* 2017;8(1):14367.
doi: 10.1038/ncomms14367
19. Mu CC, Abbott BW, Wu XD, et al. Thaw depth determines dissolved organic carbon concentration and biodegradability on the northern Qinghai-Tibetan Plateau. *Geophys Res Lett.* 2017;44(18):9389-9399.
doi: 10.1002/2017GL075067
20. Wang F, Li Z, Cheng Y, Li P, Wang B, Zhang H. Effect of thaw depth on nitrogen and phosphorus loss in runoff of loess slope. *Sustainability.* 2022;14(3):1560.
doi: 10.3390/su14031560
21. Cui F, Chen J, Liu Z, Zhu W, Wang W, Zhang W. Prediction model of thermal thawing sensibility and thaw depth for permafrost embankment along the Qinghai-Tibet engineering corridor using MODIS data. *J Sens.* 2020;2020(1):8819476.
https://doi.org/10.1155/2020/8819476
22. Agrawal K, Kumar S, Akgül A. An algorithm for numerical study of fractional atmospheric model using Bernoulli polynomials. *J Appl Math Comput.* 2024;70(4):3101-3134.
doi: 10.1007/s12190-024-02084-6
23. Yeshwanth R, Kumbinarasaiah S. Dynamics and study of atmospheric model using new modified hermite wavelet collocation method. *Iran J Sci.* 2025;49:1357-1372.
doi: 10.1007/s40995-025-01811-3
24. Naik MK, Baishya C, Veersha P, Baleanu D. Design of a fractional-order atmospheric model via a class of ACT-like chaotic system and its sliding mode chaos control. An interdisciplinary. *Chaos.* 2023, 33(2), 023129.
doi: 10.1063/5.0130403
25. Ahmed S, Jahan S, Shah K, Abdeljawad T. On computational analysis via fibonacci wavelet method for investigating some physical problems. J Appl Math Comput. 2025;71(1):531-550.
doi: 10.1007/s12190-024-02251-9
26. Khan A, Ghafoor A, Khan E, Shah K, Abdeljawad T. Solving scalar reaction diffusion equations with cubic non-linearity having time-dependent coefficients by the wavelet method of lines. *Netw Heterog Media.* 2024;19(2):634-654.
doi: 10.3934/nhm.2024028
27. Mallat SG. A theory for multiresolution signal decomposition: the wavelet representation. *IEEE Transactions on Pattern Analysis and Machine Intelligence.* 1989;11(7):674-693.
doi: 10.1109/34.192463
28. Mallat S. A Wavelet Tour of Signal Processing. *Elsevier;* 1999.
29. Kumar S, Kumar R, Agarwal RP, Samet B. A study of fractional Lotka-Volterra population model using Haar wavelet and Adams-Bashforth-Moulton methods. *Math Methods Appl Sci.* 2020;43(8):5564-5578.
doi: 10.1002/mma.6297
30. Khan NA, Ali M, Ara A, Khan MI, Abdullaeva S, Waqar M., Optimizing pantograph fractional differential equations: a Haar wavelet operational matrix method. *Partial Differ Equ Appl Math.* 2024;11:100774.
doi: 10.1016/j.padiff.2024.100774
31. Saeed U. Modified Haar wavelet method for linear and nonlinear Caputo fractional variable-order diffusion-type equations. *Eng Comput.* 2025:1-21.
https://doi.org/10.1108/EC-02-2025-0174
32. Zeb A, Kumar P, Djilali S, Erturk VS, Govindaraj V. Some novel analyses of the fractional-order COVID-19 model using the Haar wavelets method. *Int J Appl Comput Math.* 2025;11(2):36.
doi: 10.1007/s40819-025-01857-2
33. Baleanu D, Jajarmi A, Hajipour M. On the nonlinear dynamical systems within the generalized fractional derivatives with Mittag–Leffler kernel. *Nonlinear Dyn.* 2018. 94, 397-414.
doi: 10.1007/s11071-018-4367-y
34. Abdeljawad T. A Lyapunov type inequality for fractional operators with nonsingular Mittag-Leffler kernel. *J Inequal Appl.* 2017;2017(130):1-11.
doi: 10.1186/s13660-017-1400-5
35. Younis M, Ahmad H, Asmat F, Őztrk M. Analyzing Helmholtz phenomena for mixed boundary values via graphically controlled contractions. *Math Model Anal.* 2025;30(2):342–361.
doi: 10.3846/mma.2025.22546
36. Yi M, Huang J. Wavelet operational matrix method for solving fractional differential equations with variable coefficients. *Appl Math Comput.* 2014;230:383-394.
doi: 10.1016/j.amc.2013.06.102
37. ur Rehman M, Baleanu D, Alzabut J, Ismail M, Saeed U. Green–Haar wavelets method for generalized fractional differential equations. *Adv Differ Equ.* 2020;2020(515):1-25.
doi: 10.1186/s13662-020-02974-6
38. Maleknejad K, Mirzaee F, Abbasbandy S. Solving linear integro-differential equations system by using rationalized Haar functions method. *Appl Math Comput.* 2004;155(2):317-328.
doi: 10.1016/S0096-3003(03)00778-1
39. Chen CF, Hsiao CH. Haar wavelet method for solving lumped and distributed-parameter systems. *IEE Proc Control Theory Appl.* 1997;144(1):87-94.
doi: 10.1049/ip-cta:19970702

40. Storn R. On the usage of differential evolution for function optimization. *Proc North Am Fuzzy Inf Process.* 1996:519-523.
doi: 10.1109/NAFIPS.1996.534789.
41. Chen Y, Yi M, Yu C. Error analysis for numerical solution of fractional differential equation by Haar wavelets method. *J Comput Sci.* 2012;3(5):367-373.
doi: 10.1016/j.jocs.2012.04.008
42. Khan NA, Ali M, Ara A, Alraddadi I, Ahmad H. A Haar wavelet operational matrix method for fractional derivatives with non-singular kernel. *Oper Res Forum.* 2025;6(118).
doi: 10.1007/s43069-025-00502-4

Mumtaz Ali *is a lecturer at Balochistan University of Engineering and Technology, Khuzdar, Balochistan, Pakistan. He is currently pursuing a Ph.D. in Applied Mathematics at the University of Karachi. His research interests include fractional differential equations, wavelet-based numerical methods, and their applications in scientific modeling. He has published two research papers in peer-reviewed journals.*
https://orcid.org/0009-0004-3805-6808

Najeeb Alam Khan *received his Ph.D. degree in Mathematics from the University of Karachi in 2013. He is currently serving as a Professor in the Department of Mathematical Sciences, University of Karachi, Pakistan. His research interests include numerical methods, approximate analytical techniques, fluid mechanics, differential equations, fractional calculus, wavelets, and theoretical analysis. Dr. Khan has published more than 180 research papers in reputed peer-reviewed international journals.*
https://orcid.org/0000-0001-6242-0658

Muhammad Ayaz *received his Ph.D. degree from University of Karachi in 2018. He completed his Ph.D. in the field of Artificial Neural Network (ANN). His research interest areas are Mathematical modeling, fractional differential equations, and ANN.*
https://orcid.org/0009-0009-2302-9379

Nadeem Alam Khan *is an academic and researcher in Applied Mathematics and Statistics, currently associated with Iqra University, Karachi. He has held or holds the position of Associate Professor in the Computer Science Department at Iqra University. His research interests include computational mathematics, nonlinear mechanics, fractional differential equations, fluid dynamics, and applied modeling. His publication record (24 papers) spans topics in magnetohydrodynamics, fractional-order systems, nonlinear chaos, optimization methods, and flow problems.*
https://orcid.org/0009-0003-6092-5021

An International Journal of Optimization and Control: Theories & Applications
(https://accscience.com/journal/ijocta)